Linear temporal stability analysis on the inviscid sheared convective boundary layer flow

Cite as: Physics of Fluids (in press) (2022); https://doi.org/10.1063/5.0123044
Submitted: 27 August 2022 • Accepted: 26 October 2022 • Accepted Manuscript Online: 28 October 2022

Yuan Xiao, Wenxian Lin and Junling Ding

Accepted to Phys. Fluids 10.1063/5.0123044

Linear temporal stability analysis on the inviscid sheared convective boundary layer flow

Yuan Xiao (肖原),[1,2] Wenxian Lin (林文宪),[2,a)] and Junling Ding (丁俊岭)[1]

[1)] *School of Mechanotronic & Vehicle Engineering, East China Jiaotong University, Nanchang, Jiangxi 330013, China*

[2)] *College of Science & Engineering, James Cook University, Townsville, QLD 4811, Australia*

(Dated: 9 October 2022)

A linear temporal stability analysis is conducted for inviscid sheared convective boundary layer flow, in which the sheared instability with stable stratification coexists with and caps over the thermal instability with unstable stratification. The classic Taylor-Goldstein equation is applied with different stratification factors J_s and J_b in the Brunt-Väisälä frequency, respectively. Two shear-thermal hybrid instabilities, the hybrid shear stratified (HSS) and hybrid Rayleigh–Bénard (HRB) modes, are obtained by solving the eigenvalue problems. It is found that the temporal growth rates of the HSS and HRB modes vary differently with increased J_b in two distinct wavenumber ($\tilde{\alpha}$) regions defined by the intersection point between the stability boundaries of the HSS and HRB modes. Based on $J_{b,cr}$ where the temporal growth rate of the HSS and HRB are equal, a map of the unique critical boundary, which separates the effective regions of the HSS and HRB modes, is constructed and found to be dependent on J_s, J_b and $\tilde{\alpha}$. The examinations of the subordinate eigenfunctions indicate that the shear instability is well developed in the HSS mode, in which the large vortex structures may prevail and suppress the formation of convective rolls; the shear instability in the HRB mode is either 'partly developed' when $J_b < J_{b,cr}$ or 'undeveloped' when $J_b > J_{b,cr}$, thus only plays a secondary role to modify the dominant convective rolls; and as J_b increases the eigenfunctions of the HSS mode exhibit different transitional behaviors in the two regions, signifying the 'shear enhancement' and 'shear sheltering' of the entrainment of buoyancy flux.

[a)] Electronic mail: wenxian.lin@jcu.edu.au.

I. INTRODUCTION

In nature and engineering applications, sheared and thermally convective flows driven by the bulk pressure and temperature/density gradient usually coexist and interact with each other, leading to more complicated shear-thermal interactive instabilities and the associated phenomena than either the shear instability or the thermal instability alone. For instance, the Rayleigh–Bénard–Poiseuille (RBP) is a mixed-convective flow, where the shear and thermal instabilities concur in a single unstably stratified layer. Different from the pure Rayleigh–Bénard mode, in the RBP flow the transverse and longitudinal rolls may appear even at very low Rayleigh and Reynolds numbers as a result of the shear from the boundary layer flow, which also introduces the convective and absolute instabilities as well as their transitions to turbulence in the flow system[1–3]. If more than one unstably stratified layer are involved, the RBP flow becomes the stratified Rayleigh–Bénard–Poiseuille (SRBP) flow[4–6], in which the dynamics of the interface in-between different unstably stratified layers further complicates the flow system, *e.g.*, a mushroom shape interface was observed in recent work[6].

Previous studies on the shear-thermal interactive instability have focused on the scenarios where a single or multiple unstable stratified layer(s) prevail. In nature, however, a stably stratified layer could also coexist with an unstably stratified one, *e.g.*, in the atmospheric and oceanic boundary layers. In addition, the shear instabilities are not limited to the boundary layer flow either. For instance, the shear instability could initiate internally in an unbounded sheared flow, *e.g.*, the Kelvin-Helmholtz (KH) instability, which involves the prominent vortex structures with large length scales, *e.g.*, the billows and overturning waves observed in cloud and upper oceans. If the KH or other shear instabilities with large scale vortex structures coincide with the thermal instability, different hydrodynamics are highly anticipated.

Thus, the present study focuses on a different shear-thermal interactive flow, in which the sheared instability with stable stratification coexists with and caps over the thermal instability with unstable stratification. Such a shear-thermal interactive flow is called the sheared convective boundary layer (SCBL) flow by the community of the atmosphere science[7]. SCBL flows usually prevail in geophysical and atmospheric boundary layers where the entrainment and the resultant mixing processes between the stable and unstable stratified layers are significant, such as the clear atmospheric boundary layer during the fair weather

condition[8–10], the turbulent mixing in the upper ocean layer[11,12], and the water quality in reservoirs[13], among others. The understanding of the dynamics within SCBL flows is crucial for accurate modeling of complex phenomena, such as pollution dispersion[8,14,15] and clouds formation[16] in the atmospheric boundary layer. SCBL flows can also exist when the thermally unstable stratification is induced by urban regions[17–19] as an example. In addition, SCBL flows may also exist in the engineering scenarios where the shear and thermal instabilities interact in the environments where multi-stratified layers could exist, *e.g.*, the fire-induced smoke transportation[20–22], liquid metal batteries[23], petroleum industry[24] and so on.

Figure 1 shows the schematic of a typical SCBL flow usually existing in the atmospheric boundary layer, which consists of three sub-layers: the bottom unsheared stratified layer in which the thermal instability is produced by the linear unstable stratification; the middle sheared stratified layer where the shear instability is triggered from the hyperbolic profiles of the base velocity and stable stratification (it is also called the inversion layer[25,26]); and the free upper layer where the flow is unsheared and at an uniform temperature. In this study, the base flow state for the SCBL flow is selected as,

$$\left.\begin{aligned} U_*(z_*) &= \frac{\Delta u_{*,0}}{2} tanh(z_*), \quad -L < z_* \leq L, \\ \theta_*(z_*) &= \begin{cases} \dfrac{\Delta\theta_{*,0}}{2} tanh(z_*), & -L < z_* \leq L, \\ \dfrac{\Delta\theta_{*,0}}{2}\left\{-\dfrac{(\theta_b-\theta_s)}{L_b} z_* + \left[\theta_s - \dfrac{L(\theta_s-\theta_b)}{L_b}\right]\right\}, & (-L_b - L) \leq z_* \leq -L, \end{cases} \end{aligned}\right\} \quad (1)$$

where U_* is the horizontal base flow velocity in the x_* direction, θ_* is temperature, z_* is the vertical coordinate ($z_* = 0$ is at the middle height of the sheared stratified layer), L and L_b are the length scales of the stable and unstable stratifications, θ_b and θ_s represent the temperatures at the bottom heated surface and the interface, respectively, $\Delta u_{*,0}$ and $\Delta\theta_{*,0}$ represent the velocity and temperature differences across the central sheared and stratified layer, respectively. It should be mentioned that based on the function of *tanh*, the central shear stratified layer is already in the range where most of its velocity and temperature vary within $z \in [-L/2, L/2]$. Yet, to allow *tanh* function sufficiently approximating its asymptotic values, we extend the overall sheared stratified layer to $z \in [-L, L]$, which is twice of its effective length scale within $z \in [-L/2, L/2]$. The dimensionalization of perturbation equation and base flow will be presented in the next section. For the SCBL flows considered here, it is appropriate to assume the Oberbeck-Boussinesq approximation for buoyancy, so

the buoyancy is $b = \gamma\theta$, where γ is the thermal expansion coefficient, and the profile of θ is also applicable for b. The typical hyperbolic profiles of U_* and θ_* in the central sheared stratified layer allow the formation of prominent vortex structures and are commonly used in the previous studies on the pure shear stratified flow[27–34]. The linear profile of θ_* at the bottom unsheared stratified layer inherits those usually applied in the linear analysis of the pure thermal convection[35] and the convective boundary layer (CBL)[36,37]. Such a linear unstable stratification is also similar to the temperature and buoyancy flux profiles applied in the previous bulk model development for the SCBL flow as will be reviewed subsequently.

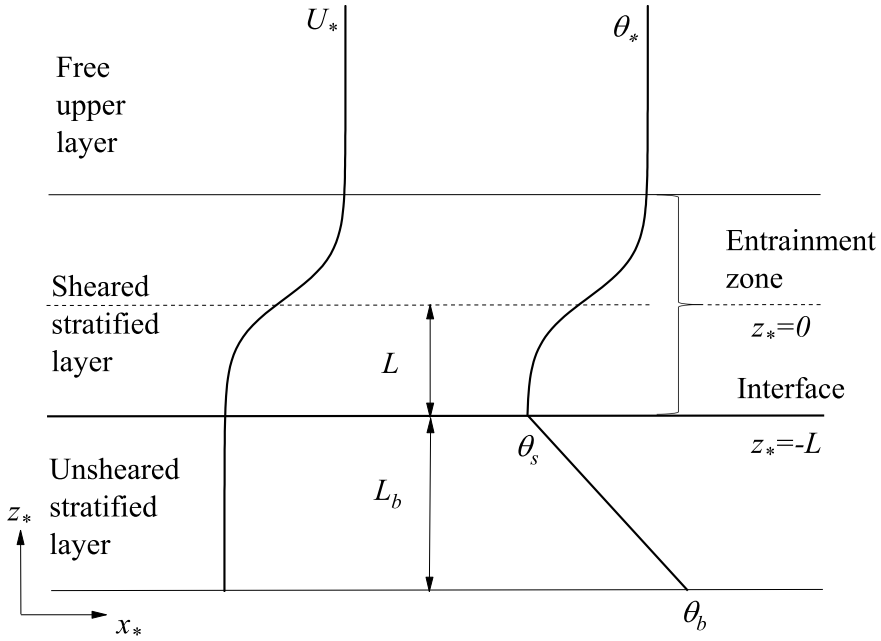

FIG. 1. Schematic of the SCBL flow represented by Eq. (1), where x_* and z_* represent the streamwise and vertical coordinate, respectively. The dash line represents the central line $z_* = 0$ of the U_* and θ_* profiles. The bold line represents the interface between the stable and unstable stratifications at $z_* = -L$.

An interface layer is formed around $z_* = -L$, with its lower end at the height in the bottom unsheared stratified layer where the temperature is the same as that in the free upper layer, which should be between θ_b and θ_s, where the uprising thermally convective flux penetrates through and further mixes into the interior of the sheared stratified layer. Reversely, the potential existences of the shear instability and stable stratification constantly modify the development of the bottom thermal instability and the entrainment of the up-

rising buoyancy flux. This interface layer and the sheared stratified layer is usually called the entrainment zone[38]. In the past decades, with field and laboratory experiments and numerical simulations, substantial studies from the atmospheric science community have been conducted for the scaling parameterization of the entrainment zone (particularly the entrainment rate) within the SCBL flow, as the entrainment zone properties are unable to be resolved by meso- and larger-scale atmospheric models. The bulk models, in which the dynamics inside the entrainment zone is parameterized in terms of velocity and buoyancy with different orders, were first proposed by Lilly[39], who considered the buoyancy and velocity jumps across the interface as the zero order model. However, it was argued that the zero order bulk model was insufficient for the SCBL flow[38,40,41], while some studies[42,43] suggested that, with proper modifications, the zero order model can still capture some essential features of the entrainment in the SCBL flow. The first order and higher order bulk models, with more complicated profiles of velocity and temperature jumps within the interface layer, have been subsequently developed[25,42–47]. In addition, the 'shear sheltering' where the shear impedes the entrainment process occasionally exists in the SCBL flow[48–50], which also complicates the applications of the bulk models in the atmospheric SCBL flow. A recent study[51] indicates that the role of the wind shear is rather dynamic, which in general depends on the relative role between the wind shear and the thermal convection in the SCBL flow.

Although the local dynamics of the entrainment zone of the SCBL flow has drawn substantial attentions, there is a significant knowledge gap regarding the global interactions between the shear and thermal instabilities in the SCBL flow. That is perhaps why, to our best knowledge, there is no report regarding the hydrodynamics of the SCBL flow, which motivates the present study to provide a global and dynamical perspective with hydrodynamic analysis. The hydrodynamics on other shear-thermal interactive instabilities have been proven to offer insightful understanding of the basic fluid dynamics and the heat/mass transfer. Previously, the hydrodynamics on the RBP flow[3,52–55] construct the map of potential instability modes and therefore guide the subsequent experimental and numerical investigations on the associated coherent structures[2,3,56]. Distinctive coherent structures associated with different instability modes may lead to different scaling correlations to be developed via experiments and numerical simulations. If the scaling parameterizations are built in a range of governing parameters involving more than one instability mode, the contradictions may appear. This is perhaps why the contradictory roles of shear, *e.g.*, 'shear

enhancement' and 'shear sheltering', were reported in the parameterization of the entrainment ratio in previous studies on SCBL flow, as reviewed, *e.g.*, in references[9,42]. Hence, we believe that the hydrodynamic analysis on the SCBL flow, even with the current invisicd linearized model, can provide certain insights to what are still unclear about the SCBL flow and guide the subsequent investigations in the future.

The other motivation for the present study is that the role of shear in the SCBL flow could be more decisive than in the RBP and SRBP flows. Indeed, in the RBP flow the effects of shear only play the secondary role as they only 'align the convective rolls along the direction of the main flow'[57], as the formations of the dominant convective rolls still depend on the thermal instability. In the SCBL flow, nevertheless, large scale vortex structures could potentially be developed by the shear from unbounded flow, therefore the shear instability has capacities to dominate over the thermal instability and even suppress the formation of convective rolls. As the large vortex structures could be developed by both the shear and thermal instabilities, the shear instability could be competitive in the SCBL flow rather than be submissive in the RBP flow. The competitive role of shear in the SCBL flow could further lead to the more complicated dynamics of the interface between the stable and unstable stratifications compared to those in the SRBP flow.

Like other shear-thermal interactive flows, the SCBL flow also involves a great number of governing parameters contributing to the overall stability. As a preliminary study on this topic, a simple but sufficient model is needed. To achieve this purpose, the present paper applies the classic Taylor-Goldstein (TG) equation[35], which is capable of capturing the inviscid sheared stratified instability, to the SCBL flow described by Eq. (1) with the special treatment by introducing different stratification factors J_s and J_b in the Brunt-Väisälä frequency for the shear and thermal instabilities, respectively. Similar strategies to introduce stable and unstable stratification factors were successfully employed in the previous hydrodynamics on the pure convective boundary layer (CBL) without shear instability[36,37]. As will be shown subsequently, the TG equation remains effective to describe both the sheared and attached thermal instabilities together in the SCBL flow. The other advantage of such a strategy is that the number of governing parameters are reduced to two, that is, J_s and J_b, which inherently quantify the interactions and competitions between the sheared and thermal instabilities. By solving the eigenvalue problems formed by the modified TG equation, the global dynamic map of two hybrid modes is revealed and distinctively different

interactive mechanisms between the shear and thermal instabilities are further elaborated with the examinations of the subordinate eigenfunctions.

This paper is organized as follows. Section II describes the derivation of the linearized perturbation equations and the special modifications for the stable and unstable stratifications. Section III provides the details of the eigenvalue/eigenfunction solver and the computational domain as well as the boundary conditions. Section IV presents the results of the eigenvalues/eigenfunctions of the SCBL flow, followed by the discussion and conclusions in Section V.

II. LINEARIZED PERTURBATION EQUATIONS

The governing equations for an inviscid, incompressible, and sheared stratified flow are:

$$\nabla_* \cdot \mathbf{u}_* = \mathbf{0}, \tag{2}$$

$$\bar{\theta}_* \frac{\partial \mathbf{u}_*}{\partial t_*} + \bar{\theta}_* (\mathbf{u}_* \cdot \nabla_* \mathbf{u}_*) = -\nabla_* p_* - g(\theta_* - \bar{\theta}_*)\vec{k}, \tag{3}$$

$$\frac{\partial \theta_*}{\partial t_*} + \mathbf{u}_* \cdot \nabla_* \theta_* = 0, \tag{4}$$

where the subscript '*' denotes the dimensional quantities, $\mathbf{u}_*$ is the velocity vector with the components (u_*, v_*, w_*) in the Cartesian coordinates (x_*, y_*, z_*), p_* is pressure, θ_* is temperature, $\bar{\theta}_*$ is the reference temperature, t_* is time, and g is the acceleration due to gravity, respectively.

The above equations can be made dimensionless as follows,

$$\nabla \cdot \mathbf{u} = 0, \tag{5}$$

$$\bar{\theta} \frac{\partial \mathbf{u}}{\partial t} + \bar{\theta}(\mathbf{u} \cdot \nabla \mathbf{u}) = -\nabla p - \frac{(\theta - \bar{\theta})}{Fr^2}\vec{k}, \tag{6}$$

$$\frac{\partial \theta}{\partial t} + \mathbf{u} \cdot \nabla \theta = 0, \tag{7}$$

where the dimensional quantities are made dimensionless using their respective characteristic scales, *i.e.*,

$$\mathbf{x} = \frac{\mathbf{x}_*}{L_c}, \quad t = \frac{t_*}{(L_c/V_c)}, \quad \mathbf{u} = \frac{\mathbf{u}_*}{V_c}, \quad p = \frac{p_*}{\Delta\rho_* V_c^2}, \quad \theta = \frac{\theta_*}{\Delta\theta_*}, \quad \bar{\theta} = \frac{\bar{\theta}_*}{\Delta\theta_*}, \tag{8}$$

in which $\mathbf{x}$ is the dimensionless coordinate vector ($x\vec{i}+y\vec{j}+z\vec{k}$) where $\vec{i}$, $\vec{j}$ and $\vec{k}$ represent the unit vectors in the x, y and z directions, $\mathbf{u}$ is the dimensionless velocity vector ($u\vec{i}+v\vec{j}+w\vec{k}$),

L_c, V_c, $\Delta\rho_*$ and $\Delta\theta_*$ are the characteristic length, velocity, density and temperature scales, respectively. In the present study, L_c, V_c and $\Delta\theta_*$ are selected as $L/2$, $\Delta u_{*,0}/2$ and $\Delta\theta_{*,0}/2$ (whose definition refer to Eq.(1)), respectively. Such selections are based on the velocity and temperature variations across the half of central sheared stratified layer, which was usually applied in previous studies on shear stratified layer.

Fr in Eq. (6) is the Froude number which is defined by,

$$Fr = \frac{V_c}{\sqrt{gL}}.$$

With dimensionless properties in Eq.(8), the dimensionless form of the base flow Eq.(1) is:

$$\left.\begin{aligned} U(z) &= tanh(z), \quad -2 < z \leq 2, \\ \theta(z) &= \begin{cases} tanh(z), & -2 < z \leq 2, \\ -\dfrac{(\theta_b - \theta_s)}{L_b} z + [\theta_s - \dfrac{L(\theta_s - \theta_b)}{L_b}] & (-\dfrac{2L_b}{L} - 2) \leq z \leq -2, \end{cases} \end{aligned}\right\} \tag{9}$$

It is assumed that the flow quantities consist of the basic flow and infinitesimal perturbations:

$$\mathbf{u}(\mathbf{x}, t) = \mathbf{U}(z) + \mathbf{u}'(\mathbf{x},t), \tag{10}$$

$$\theta(\mathbf{x}, t) = \theta_b(z) + \theta'(\mathbf{x},t), \tag{11}$$

$$p(\mathbf{x}, t) = P(z) + p'(\mathbf{x}, t) = p_0 - \frac{1}{Fr^2}\int_0^z \theta_b(z)dz + p'(\mathbf{x}, t), \tag{12}$$

where $\mathbf{U}(z)$ is the dimensionless basic flow velocity, $\theta_b(z)$ is the dimensionless basic temperature profile, and p_0 is the dimensionless reference pressure corresponding to the dimensionless reference temperature $\bar{\theta}$. The superscript symbol '$'$' represents the perturbation part of the corresponding physical property.

For the sheared stratified flows considered in this paper, the base flow is assumed to be in the x-direction and to vary with the vertical coordinate z only, *i.e.*,

$$\mathbf{U}(z) = U(z)\vec{i}. \tag{13}$$

With this, the following perturbation equations can be deduced (the details are presented in Appendix A),

$$\frac{\partial u'}{\partial x} + \frac{\partial v'}{\partial y} + \frac{\partial w'}{\partial z} = 0, \tag{14}$$

$$\bar{\theta}\frac{\partial u'}{\partial t} + \bar{\theta}U(z)\frac{\partial u'}{\partial x} + \bar{\theta}w'\frac{\partial U(z)}{\partial z} = -\frac{\partial p'}{\partial x}, \tag{15}$$

$$\bar{\theta}\frac{\partial v'}{\partial t} + \bar{\theta}U(z)\frac{\partial v'}{\partial x} = -\frac{\partial p'}{\partial y}, \tag{16}$$

$$\bar{\theta}\frac{\partial w'}{\partial t} + \bar{\theta}U(z)\frac{\partial w'}{\partial x} = -\frac{\partial p'}{\partial z} - \frac{\theta'}{Fr^2}, \tag{17}$$

$$\frac{\partial \theta'}{\partial t} + U(z)\frac{\partial \theta'}{\partial x} + w'\frac{\partial \theta_b(z)}{\partial z} = 0. \tag{18}$$

The following normal mode is used in the subsequent linear temporal stability analysis,

$$\phi'(\mathbf{x}, t) = \hat{\phi}(z)e^{i(\alpha x+\beta y)-i\alpha ct} = \hat{\phi}(z)e^{i(\alpha x+\beta y)+\sigma t}, \tag{19}$$

where i is the imaginary unit of a complex number, α and β are the wavenumbers in the x and y directions respectively, and the perturbation quantity ϕ' represents velocity, density, temperature, buoyancy flux, or other physical quantities. The hat symbol ('$\hat{}$') denotes the peak amplitude of the corresponding perturbation. c is the wave (phase) speed, which gives $\omega = \alpha c$ as the angular frequency for the perturbation, and $\sigma = -i\alpha c$ as the temporal growth rate of the perturbation.

Substituting the above normal modes into Eqs. (14)-(18) leads to the following,

$$i\alpha\hat{u} + i\beta\hat{v} + D\hat{w} = 0, \tag{20}$$

$$\bar{\theta}(i\alpha U + \sigma)\hat{u} + \bar{\theta}U_z\hat{w} = -i\alpha\hat{p}, \tag{21}$$

$$\bar{\theta}(i\alpha U + \sigma)\hat{v} = -i\beta\hat{p}, \tag{22}$$

$$\bar{\theta}(i\alpha U + \sigma)\hat{w} = -D\hat{p} - \frac{\hat{\theta}}{Fr^2}, \tag{23}$$

$$(i\alpha U + \sigma)\hat{\theta} + \theta_{b,z}\hat{w} = 0, \tag{24}$$

where $D = \partial/\partial z$ is the differential operator for the perturbation properties, $\theta_{b,z} = \partial\theta_b(z)/\partial z$, and the subscript '$z$' denotes the first order differentiation with respect to z.

As shown in Appendix B, by applying the Squire transformations[35,58], the three-dimensional perturbation equations Eqs. (20)-(24) can be reduced to the following equivalent two-dimensional perturbation equations, which are written in matrix form,

$$\tilde{\sigma}\begin{bmatrix} \nabla_s^2 & \\ & I \end{bmatrix}\begin{bmatrix} \hat{w} \\ \tilde{\theta} \end{bmatrix} = \begin{bmatrix} -i\tilde{\alpha}(U\nabla_s^2 - U_{zz}) & \dfrac{\tilde{\alpha}^2}{\bar{\theta}Fr^2} \\ -\tilde{\theta}_{b,z} & -i\tilde{\alpha}U \end{bmatrix}\begin{bmatrix} \hat{w} \\ \tilde{\theta} \end{bmatrix}, \tag{25}$$

where

$$\tilde{\alpha} = (\alpha^2 + \beta^2)^{1/2}, \quad \tilde{u} = \frac{\alpha\hat{u} + \beta\hat{v}}{\tilde{\alpha}}, \quad \tilde{\theta}_{b,z} = \theta_{b,z}\frac{\tilde{\alpha}^2}{\alpha^2},$$

$$\tilde{p} = \frac{\tilde{\alpha}}{\alpha}\hat{p}, \quad \tilde{\theta} = \frac{\tilde{\alpha}}{\alpha}\hat{\theta}, \quad \tilde{\sigma} = \sigma\frac{\tilde{\alpha}}{\alpha}, \quad \nabla_s^2 = D^2 - \tilde{\alpha}^2,$$

in which the tilde symbol '~' denotes the Squire transformation properties. For stratified flows, $\tilde{\theta}_{b,z}$ represents the profiles of stratification. If the Squire buoyancy $\tilde{b} = \tilde{\theta}/\bar{\theta}$ is used instead of the Squire temperature $\tilde{\theta}$, the above perturbation equations will become,

$$\tilde{\sigma}\begin{bmatrix} \nabla_s^2 & \\ & I \end{bmatrix}\begin{bmatrix} \hat{w} \\ \tilde{b} \end{bmatrix} = \begin{bmatrix} -i\tilde{\alpha}(U\nabla_s^2 - U_{zz}) & \dfrac{\tilde{\alpha}^2}{Fr^2} \\ \tilde{N}^2 & -i\tilde{\alpha}U \end{bmatrix}\begin{bmatrix} \hat{w} \\ \tilde{b} \end{bmatrix}, \tag{26}$$

where $\tilde{N}^2 = -\tilde{\theta}_{b,z}/\bar{\theta}$ is the local Squire buoyancy Brunt-Väisälä frequency. For unstratified flows, simply letting $\tilde{\theta}_{b,z} = 0$ in Eq. (25) or $\tilde{N}^2 = 0$ in Eq. (26) will give the corresponding perturbation equations.

As suggested by Hazel[59], a stratification factor $J_s = N^2(z)/(\partial\theta/\partial z)$ when $z > -2$, can be used to represent the intensity of the central stable stratification of the SCBL flow. Particularly, if both the velocity and background stratification of the base flow satisfy $(\partial u/\partial z)|_{z=0} = sech^2(z)|_{z=0} = 1$ and $(\partial\theta/\partial z)|_{z=0} = sech^2(z)|_{z=0} = 1$, where $z = 0$ is at the middle height of the sheared stratified layer, the local Richardson number $Ri_g(z)$:

$$Ri_g(z) = \frac{N^2(z)}{[(\partial u/\partial z)|_{z=0}]^2} = J_s\frac{(\partial\theta/\partial z)|_{z=0}}{[(\partial u/\partial z)|_{z=0}]^2} = J_s. \tag{27}$$

Thus, as the base flow state u and θ in Eq. (1) satisfy $(\partial u/\partial z)|_{z=0} = 1$ and $(\partial\theta/\partial z)|_{z=0} = 1$, J_s plays as an effective substitute for Ri_g that is usually employed in the studies of the sheared stratified flow.

In penetrative convection problems where a thermal convection region is capped by a stably stratified layer without sheared instability, Whitehead and Chen[36] and Sun[37] introduced a stability factor S to quantify the stable stratification similar to the Rayleigh number (Ra). Inspired by this method, in the present invicid SCBL flow, we similarly propose the unstable stratification factor J_b to quantify the unstable stratification associated with the thermal instability, so that $N^2(z)$ is also divided into stable and unstable region as:

$$N^2(z) = \begin{cases} J_s\dfrac{\partial\theta}{\partial z}, & -2 < z \leq 2, \\ J_b\dfrac{\partial\theta}{\partial z}, & (-\dfrac{2L_b}{L} - 2) \leq z \leq -2, \end{cases} \tag{28}$$

where $\partial\theta/\partial z$ is determined by $\theta(z)$ in Eq.(1). Together with J_s and J_b, both the stable and unstable stratification are incorporated in $N^2(z)$ and therefore in the linear analysis. Specially once $u = 0$ or the sheared instability is suppressed by overly stable stratification, the SCBL flow will become the pure CBL flow.

III. METHODOLOGY

The temporal mode of the eigenvalue problems is solved with the matrix methods. The linearized perturbation equation (26) is uniformly discretized by using the second-order central difference scheme. The QZ algorithm developed by Moler and Stewart[60], which is integrated in the LAPACK routine CGGEV, is used as the complex eigenvalue solver. The robustness of the QZ algorithm in the hydrodynamic stability analysis has been demonstrated in some studies[61–65]. With the QZ algorithm, solving the eigenvalue equation (26) also obtains $\hat{w}$. As both σ and $\hat{w}$ are solved, the rest unknown eigenfunctions $\hat{u}$ and $\hat{p}$ are solved with the equations (20)-(22) using the solver ZSYSV integrated in the LAPACK. Then $\hat{\omega}_y = D\hat{u} - i\alpha\hat{w}$ is able to be solved.

The boundary conditions $u = w = 0$ are applied at both the top and the bottom boundaries, and $b = b_b$ is applied at the bottom boundary, where b_b is adjusted based on the values of selected J_b for each run. The dimensionless vertical coordinate z varies between -5 and 5, giving the corresponding dimensional computational domain a size ten times of the characteristic length of the central sheared instability. The resolution with node numbers of $600 \sim 2000$ as well as the dimensionless computational domain sizes between 10 and 50 are tested, with less than 1% variations observed. Thus 10 is selected as the dimensionless computational size along with the node number of 600, which is sufficiently large to capture the asymptotic hydrodynamic behaviors obtained in other settings with the much larger domain sizes and many more node numbers. The influences of L_b is also tested as shown in Appendix C. To ensure the occurrences of all hybrid modes and the constant growth rate of the hybrid shear stratified mode (defined in Section IV), L_b is fixed at 3 (60% of one half domain as $L + L_b = 5$) in the subsequent results.

IV. RESULTS

Before presenting the results of eigenvalues/eigenfunctions, it is helpful to illustrate the hybrid instabilities in the SCBL flow frequently referred to subsequently in the present study, as schematically depicted in Fig. 2 with the flow configuration presented in Fig. 1. In the sheared stratified layer, once the velocity shear overcomes the stable stratification, the perturbed vorticity gradually grows and develops into coherent structures (*e.g.*, Kelvin-

Helmholtz (KH) eddies), *i.e.*, the sheared stratified instability as denoted by 'SS'. In the unsheared stratified layer, once the thermal convection exceeds a certain critical level (Ra for viscous flows and J_b for the current invicid flow), the thermal convective flux will constantly arise, develop and even penetrate through the interface, *i.e.*, the thermal or the Rayleigh-Bénard instability as denoted by 'RB'. In reality the critical condition for the thermal instability is usually easy to be satisfied, therefore once the sheared instability occurs, it will always coexist with the thermal instability in the SCBL flow, inherently giving the SCBL flow the hybrid features between the SS mode and the RB mode. If the sheared instability can completely develop into coherent vortex KH eddies under the insufficient influences of the thermal instability, the corresponding hybrid mode may be dominated by the features of the SS mode and therefore is appropriately named as the 'hybrid sheared stratified' (HSS) mode. On the contrary, if the sheared instability is only partly developed or even completely destroyed by the stronger penetrative thermal flux, yet the thermal instability is still modified by the undeveloped sheared instability or directly by the stably stratification, such a hybrid mode is appropriately named as the 'hybrid thermal' or 'hybrid Rayleigh-Bénard' (HRB)' mode as the thermal or the Rayleigh-Bénard instability dominates.

A. Eigenvalues

By solving the eigenvalue problems defined by Eq. (26), it is found that the HSS and HRB modes can be clearly identified by the temporal growth rate $\tilde{\sigma}$. The HSS mode involves negligible $\mathrm{Im}[\tilde{\sigma}]$ compared to $\mathrm{Re}[\tilde{\sigma}]$, where Re and Im represent the real and imaginary parts of a complex number, respectively, indicating that the instability mode is stationary with regard to the base flow. Such a stationary feature agrees well with the pure SS mode without the thermal instability at the bottom, which suggests that the name 'HSS' mode is appropriate. The HRB mode involves significant $\mathrm{Im}[\tilde{\sigma}]$, indicating that the corresponding instability propagates away from the base flow, which also suggests that the name 'HRB' mode is appropriate.

Based on the distinctions of $\mathrm{Im}[\tilde{\sigma}]$ between the HRB and HSS modes mentioned above, Figure 3 delineates the stability boundaries of the HSS mode in terms of J_s versus $\tilde{\alpha}$ and the HRB mode in terms of J_b versus $\tilde{\alpha}$, respectively. It is found that the stability boundary of the HSS mode is independent of J_b and only depends on J_s, therefore the approximately

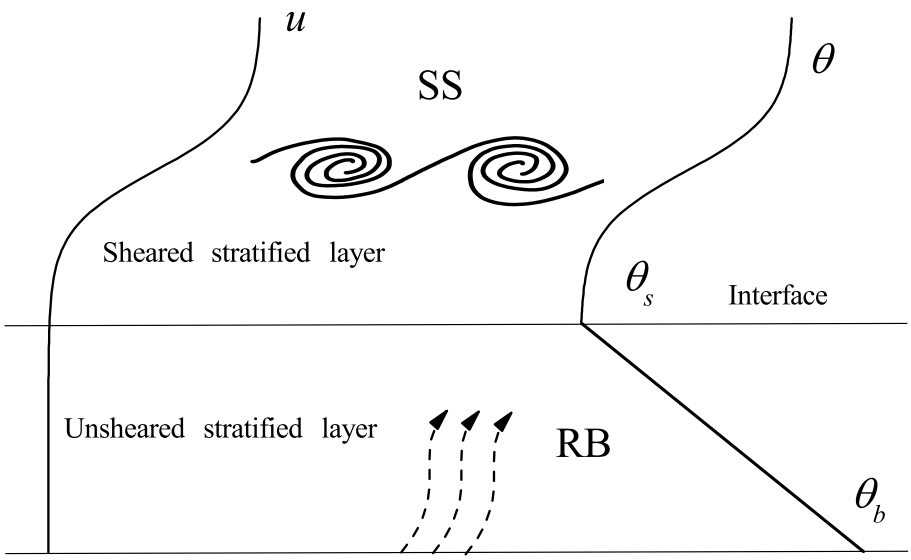

FIG. 2. Schematic of the instabilities in the SCBL flow (Eq. (1)). 'SS' and 'RB' represent the sheared stratified and the thermal (Rayleigh-Benard) instabilities, respectively.

arc shaped boundary of the pure sheared stratified flow in terms of J_s versus $\tilde{\alpha}$, as reported previously[35,59,66,67], is reproduced. Yet, the subordinate eigenfunctions of the HSS mode is different, as they involve the features from the RB mode. On the other hand, the stability boundary of the HRB mode reproduces the hyperbolic shape as solved by the classic viscous model[35], indicating that the inviscid TG equation with the unstable stratification is sufficient to capture the essential features of the thermal convective instability. Unlike the HSS mode, the stability boundary of the HRB mode depends on J_s, as the unstable regions of the HRB mode gradually shrink as J_s increases. Nevertheless, such dependency appears only obvious once J_s is more than the critical value $J_{s,cr} = 0.25$, below which the HSS mode exists. Likewise, the eigenfunctions of the HRB mode also involve the features of the SS mode, thus, are different from that of the pure RB mode.

As the stability boundary of the HSS mode is independent of J_b, the entire unstable region of the HSS mode therefore appears as a 'column' in the three-dimensional (J_s, J_b, $\tilde{\alpha}$) space. The base area of the 'column' is the unstable region of the HSS mode plotted in Fig. 3

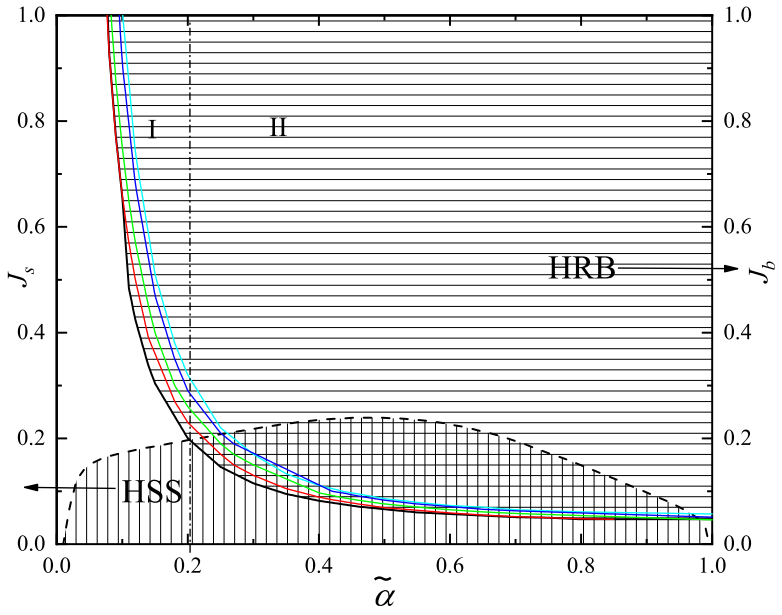

FIG. 3. The stability boundaries of the HSS mode (dashed curve line) as a function of J_s and the Squire wavenumber $\tilde{\alpha}$ and the HRB mode (solid curve lines) as a function of J_s, J_b and the Squire wavenumber $\tilde{\alpha}$. The unstable regions for the HSS and HRB modes bounded by their respective stability boundaries are marked with vertical and horizontal grids, and the mesh region is the coinciding unstable regions of the HSS and HRB modes, respectively. The stability boundaries of the HRB modes at $J_s = 0$, 0.5, 1.0, 3 and 6, are presented with (—), (—), (—), (—) and (—) curve lines, respectively.

and its height infinitely extends along the J_s axis. Such a 'column' inevitably intersects with the unstable region of the HRB mode, which appears like a 'cone' in the three-dimensional (J_s, J_b, $\tilde{\alpha}$) space, because the unstable region of the HRB mode gradually decreases with increased J_s as shown in Fig. 3. The intersection line between the 'column' and the 'cone' in the three-dimensional (J_s, J_b, $\tilde{\alpha}$) space is projected in the (J_s, $\tilde{\alpha}$) plane shown in Fig. 3, in the form of the track of several intersection points between the stability boundaries of the HSS and HRB modes. Based on the intersection point, *e.g.*, the one at $\tilde{\alpha} \approx 0.2$, the entire map is separated into two regions: Region I and II, as highlighted by the vertical dashed-dot line in Fig. 3. In Region II, the HRB mode can easily survives as long as $J_b > 0.07$, a trivial value that can be easily satisfied in reality similar to $Ra_{cr} \approx 1700$.[35] Thus in Region II, as long as the HSS mode exists, the two hybrid modes always compete with each other. In

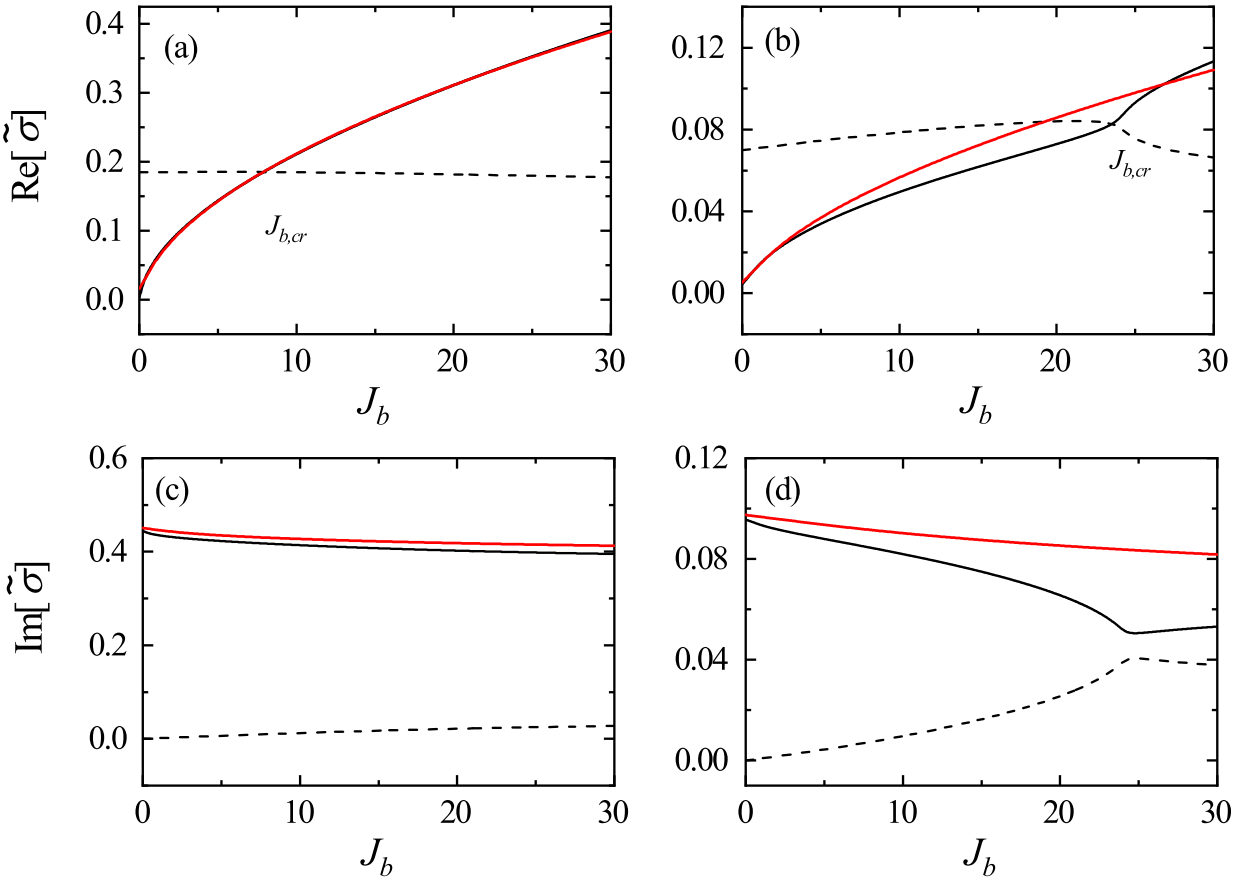

FIG. 4. The real and imaginary parts of $\tilde{\sigma}$ plotted against J_b at $\tilde{\alpha} = 0.46$ ((a) and (c)) and $\tilde{\alpha} = 0.1$ ((b) and (d)) with $J_s = 0$. The solutions of the HSS and the HRB modes are denoted by the dashed and solid lines, respectively. $J_{b,cr}$ where the branches of $\mathrm{Re}[\tilde{\sigma}]_{\mathrm{HSS}}$ and $\mathrm{Re}[\tilde{\sigma}]_{\mathrm{HRB}}$ intersect is denoted for $\tilde{\alpha} = 0.46$ and 0.1 in (a) and (b), respectively. For comparison, the real and imaginary part of $\tilde{\sigma}$ against J_b at $J_s = 0.5$ (pure RB mode) are also plot in (—).

Region I, as the HRB mode must occur at $J_b \gtrsim 0.2$, there is a significant gap where the HSS mode can exist yet the HRB mode is absent. In addition, distinctively different behaviors of the HSS and the HRB modes are observed in Region I and II as will be shown later.

Away from the stability boundaries, the complex temporal growth rates ($\tilde{\sigma}$) for both the HSS and HRB modes exhibit strong dependency on both J_s and J_b. Figure 4 presents the real and imaginary parts of $\tilde{\sigma}$ for the HSS (—) and HRB (- - -) modes with $J_s = 0$ and $\tilde{\alpha} = 0.1$ in Region I and 0.46 in Region II, respectively. For comparison, $\tilde{\sigma} \sim J_b$ plots (—) for the pure RB mode are also included, with $J_s = 0.5 > J_{s,cr} = 0.25$ which completely

eliminates the shear instability. For other $\tilde{\alpha}$ values in Regions I and II of the hybrid modes, the results are highly similar to $\tilde{\alpha} = 0.1$ and 0.46 respectively and thus are not presented here. It is also found that for non-zero J_s values, $\mathrm{Re}[\tilde{\sigma}]$ versus J_b and $\mathrm{Im}[\tilde{\sigma}]$ versus J_b exhibit very similar fashions to those for $J_s = 0$ as shown in Fig. 4, and are therefore not presented here either. For convenience, the subscripts 'HSS' and 'HRB' are applied to $\mathrm{Re}[\tilde{\sigma}]$ and $\mathrm{Im}[\tilde{\sigma}]$ as well, *e.g.*, $\mathrm{Re}[\tilde{\sigma}]_{\mathrm{HSS}}$ and $\mathrm{Re}[\tilde{\sigma}]_{\mathrm{HRB}}$ represent $\mathrm{Re}[\tilde{\sigma}]$ for the HSS mode and the HRB mode, respectively. In addition, the critical J_b value at which $\mathrm{Re}[\tilde{\sigma}]_{\mathrm{HSS}}$ is equal to $\mathrm{Re}[\tilde{\sigma}]_{\mathrm{HRB}}$, is defined as a specific critical condition $J_{b,cr}$, with the subscript 'cr' indicates the critical condition where the HSS mode and the HRB mode are equally weighted in the SCBL flow.

At $\tilde{\alpha} = 0.46$, as shown in Fig. 4(a) and (c), $\mathrm{Re}[\tilde{\sigma}]_{\mathrm{HSS}}$ is almost constant (at about 0.18) when J_b increases, though slight variations are still observed; correspondingly, $\mathrm{Im}[\tilde{\sigma}]_{\mathrm{HSS}}$ gradually but very slightly increases when J_b increases, yet its overall magnitudes are still insignificant compared to that of $\mathrm{Re}[\tilde{\sigma}]_{\mathrm{HSS}}$, indicating that the HSS mode remains the stationary feature. Similar to what have been observed for $\tilde{\alpha} = 0.46$, at every $\tilde{\alpha}$ value in Region II, all HSS modes share the similar stable stationary feature exhibited in Fig. 4(a) and (c), therefore it seems that the HSS mode is overall insensitive to J_b in Region II. Nevertheless, this is only partly true as will be shown later in the subsequent examination of the subordinate eigenfunctions. In contrast, as shown in Fig. 4(a) and (c), the profiles of the HRB and pure RB mode almost overlap, suggesting that the HRB mode involve similar strong propagative feature as the pure RB mode. Yet, the HRB and pure RB mode are not completely the same in their subordinate eigenfunctions as will be shown later.

At $\tilde{\alpha} = 0.1$ in Region I, as shown in Fig. 4(b) and (d), however, $\mathrm{Re}[\tilde{\sigma}]$ and $\mathrm{Im}[\tilde{\sigma}]$ for both the HRB and HSS mode vary significantly with the increase of J_b, especially with their inflection points both occur at $J_{b,cr}$. Particularly, Fig. 4(d) shows that $\mathrm{Im}[\tilde{\sigma}]_{\mathrm{HSS}}$ increases significantly until at $J_{b,cr}$ when J_b increases, implying that the HSS mode gradually possesses the propagtive features instead of the stationary ones; on the contrary, $\mathrm{Im}[\tilde{\sigma}]_{\mathrm{HRB}}$ remarkably declines with increased J_b until $J_{b,cr}$ and then slowly increases again.

Due to such almost opposite trends between $\mathrm{Im}[\tilde{\sigma}]_{\mathrm{HSS}}$ and $\mathrm{Im}[\tilde{\sigma}]_{\mathrm{HRB}}$ with increased J_b the branches of $\mathrm{Im}[\tilde{\sigma}]_{\mathrm{HSS}}$ and $\mathrm{Im}[\tilde{\sigma}]_{\mathrm{HRB}}$ gradually come close to each other when J_b increases until $J_{b,cr}$, indicating that the two hybrid modes may share some common structures, which will also be further verified in the subsequent examination of the eigenfunctions.

As shown above in Fig. 4, for a specific J_s value, each $\tilde{\alpha}$ could yield one $J_{b,cr}$ by identifying

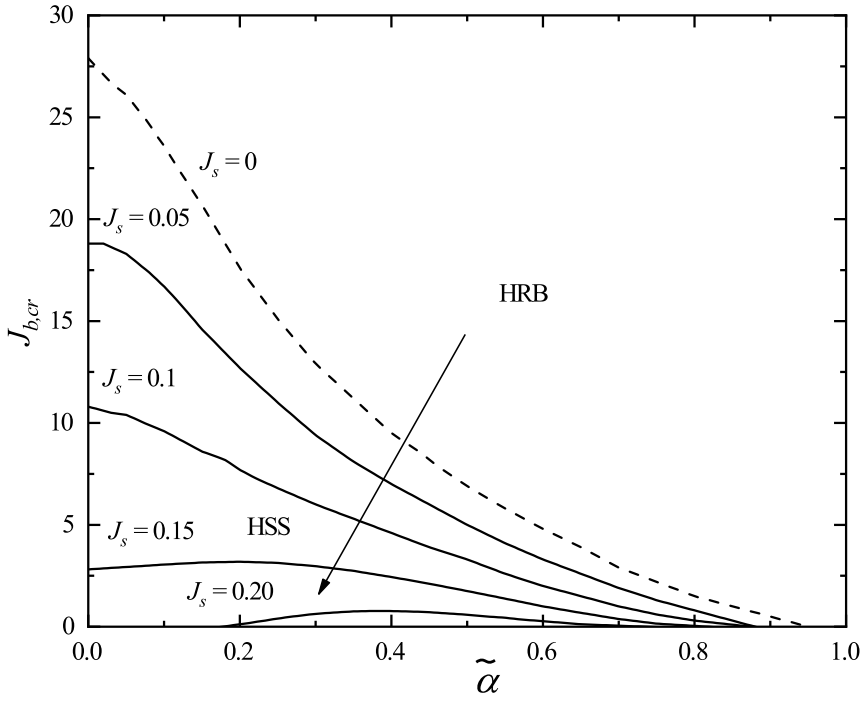

FIG. 5. The boundary of $J_{b,cr}$, which distinguishes the HSS mode and the HRB mode, plotted against $\tilde{\alpha}$ for $J_s = 0$, 0.05, 0.1, 0.15 and 0.2, respectively. The boundary of $J_{b,cr}$ for $J_s = 0$ is highlighted with the dashed line, while those for other J_s values are plot with the solid lines. For each J_s boundary, 'HRB' denotes the dominant region of the HRB mode which is above the boundary, while 'HSS' represents the dominant region of the HSS mode which is below the boundary. The arrow indicates the expansion of the dominant region of the HRB mode as J_s increases.

the intersection point, so that after collecting a series of $J_{b,cr}$ at different $\tilde{\alpha}$, an unique critical boundary representing the competitions between the HRB and HSS modes in the SCBL flow could be constructed. Figure 5 plots such boundaries for $J_s = 0$, 0.05, 0.1, 0.15 and 0.2, where the region above the boundary signifies the domination of the HRB mode over the HSS mode, while the region below indicates the opposite. The figure shows that as J_s increases the dominant regions of the HRB mode expand, while, correspondingly, that of the HSS mode shrinks. As the maximum value of $\mathrm{Re}[\tilde{\sigma}]_{\mathrm{HSS}}$ always occurs at the unstratified condition when $J_s = 0$, it is apparent that when $J_s = 0$ the region dominated by the HRB mode is the minimum while that dominated by the HSS mode is the maximum for all J_s values. It is found that when $J_s > 0.25$, the region dominated by the HSS mode

essentially disappears, implying that it is completely suppressed by the overly stable central stratification, so that the dominant region of the HRB mode occupies the entire domain of $\tilde{\alpha}$. For this extreme case, the boundary of $J_{b,cr}$ can be considered as the $\tilde{\alpha}$ axis itself (*i.e.*, $J_{b,cr} \approx 0$ for all $\tilde{\alpha}$ values).

From Fig. 5, it is noted that the shapes of the critical boundaries of $J_{b,cr}$ versus $\tilde{\alpha}$ are also different in Regions I and II. This is because the branches $\mathrm{Re}[\tilde{\sigma}]_{\mathrm{HSS}}$ and $\mathrm{Re}[\tilde{\sigma}]_{\mathrm{HRB}}$ behave differently, as shown in Fig. 4. In Region I with $\tilde{\alpha} \lesssim 0.2$, the values of $J_{b,cr}$ are significantly larger than that in Region II for a specific J_s value when $J_s \geq 0.1$, and the reductions of $J_{b,cr}$ in Region I are also substantial. This is because the occurrence of $J_{b,cr}$ as the intersection point where the branches of $\mathrm{Re}[\tilde{\sigma}]_{\mathrm{HSS}}$ and $\mathrm{Re}[\tilde{\sigma}]_{\mathrm{HRB}}$ intersect, is remarkably postponed by the rising branch of $\mathrm{Re}[\tilde{\sigma}]_{\mathrm{HSS}}$ as J_b increase, as shown in Fig. 4(a). Furthermore, as $\tilde{\alpha}$ increases, the value of $J_{b,cr}$ decreases monotonically in Region II, as the branch of $\mathrm{Re}[\tilde{\sigma}]_{\mathrm{HSS}}$ gradually becomes constant, so that $J_{b,cr}$ depends only on the growth of $\mathrm{Re}[\tilde{\sigma}]_{\mathrm{HRB}}$, like that observed in Fig. 4(a). Nevertheless, in Region I, the relations between $J_{b,cr}$ and $\tilde{\alpha}$ are not monotonically for all J_s values. Overall, the critical boundary of $J_{b,cr}$ and its dependence on J_s strongly suggest that the competition between the HSS mode and the HRB mode dynamically depends on J_s, J_b and $\tilde{\alpha}$ all together.

B. Eigenfunctions

It is necessary to examine the eigenfunctions of the pure SS mode with the shear stratified instability only and the pure RB mode with the thermal instability only, before exhibiting the eigenfunctions of the HRB and HSS modes which inevitably include the hybrid features of the shear and thermal instabilities all the time. Figures 6 and 7 present the eigenfunctions for the pure SS mode with $J_b = 0$ and $J_s = 0.1$ and for the pure RB mode with $J_s = 0.5$, with a series of increased J_b that gradually approach then exceed $J_{b,cr}$ at $\tilde{\alpha} = 0.1$ and 0.46, respectively. As $J_b = 0$ eliminates the bottom unstable stratification and $J_s = 0.5 > J_{s,cr} = 0.25$ indicates that the overly stable stratification suppresses the shear instability, the selected parameters in both figures ensure that the shear and thermal instabilities isolate from each other. For the subsequent comparisons for the HRB mode in Figs. 8 and 9, a series of the same J_b values are also selected for the pure RB mode in Figs. 6 and 7, respectively.

In Figs. 6 and 7, the pure SS and RB modes distinguish each other in the following aspects.

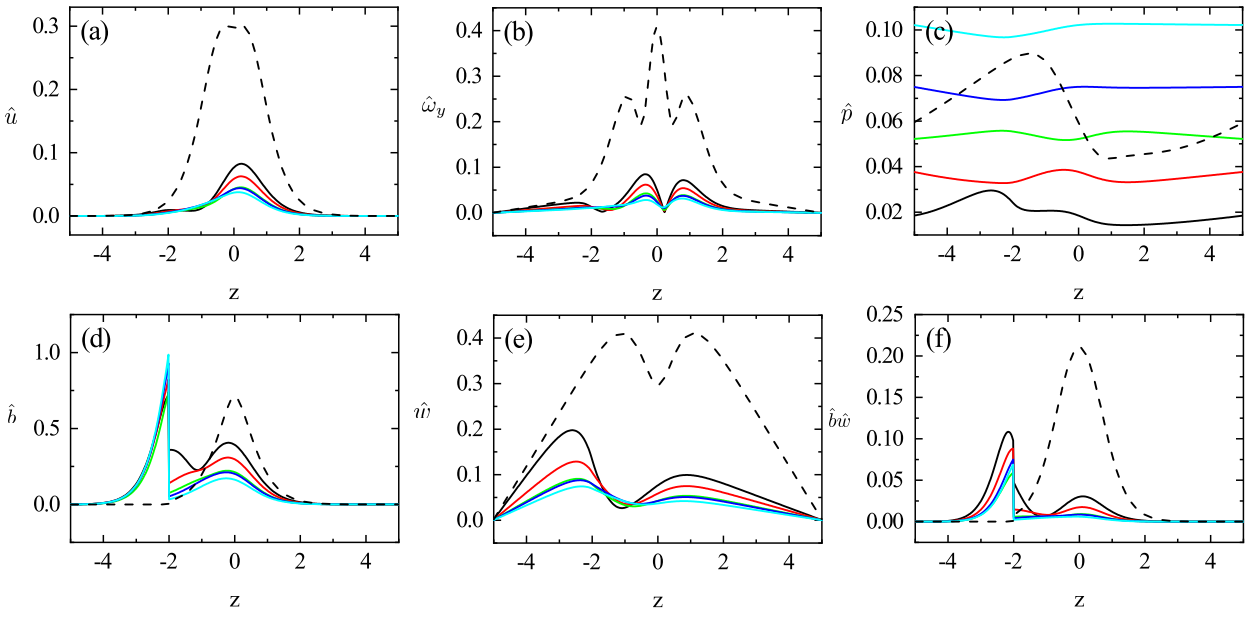

FIG. 6. The profiles of the absolute values of (a) $\hat{u}$, (b) $\hat{\omega}_y$, (c)$\hat{p}$, (d) $\hat{b}$, (e) $\hat{w}$, and(f) $\hat{b}\hat{w}$ in the z direction at $\tilde{\alpha} = 0.1$ for the pure SS mode with $J_b = 0$ and $J_s = 0.1$ (dash lines) and the pure RB mode with $J_s = 0.5$ and $J_b = 1.0$ (—), 3.0 (—), 5.0 (—), 9.0 (—) and 15.0 (—), respectively.

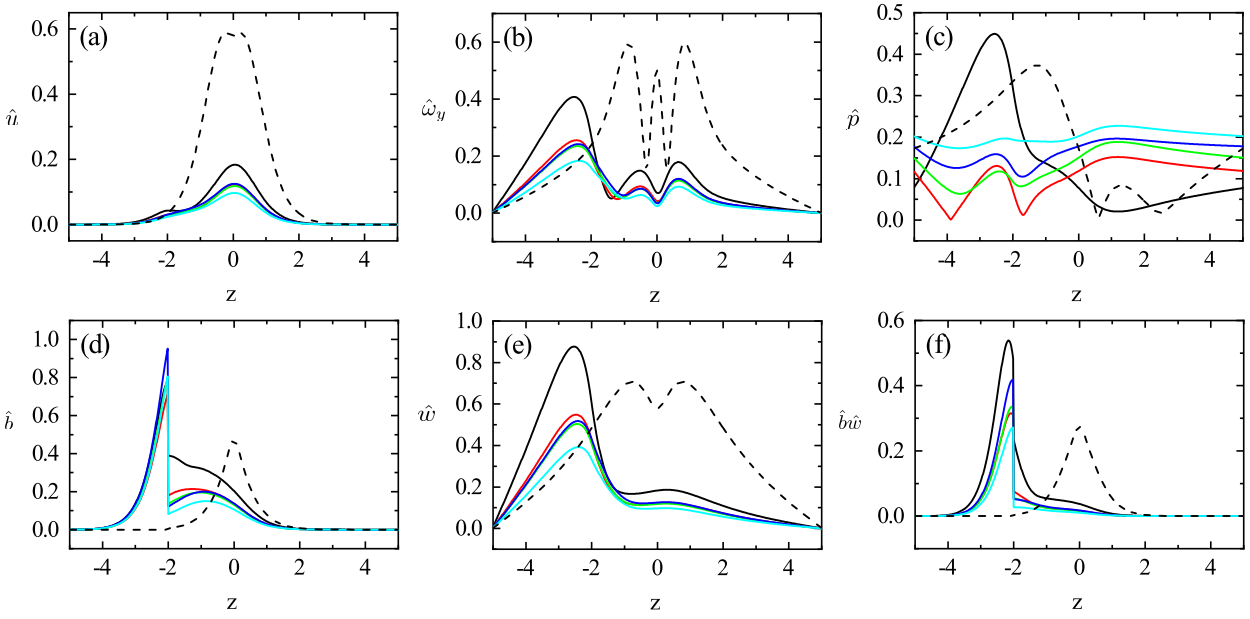

FIG. 7. The profiles of the absolute values of (a) $\hat{u}$, (b) $\hat{\omega}_y$, (c)$\hat{p}$, (d) $\hat{b}$, (e) $\hat{w}$, and(f) $\hat{b}\hat{w}$ in the z direction at $\tilde{\alpha} = 0.46$ for the pure SS mode with $J_b = 0$ and $J_s = 0.1$ (dash lines) and the pure RB mode with $J_s = 0.5$ and $J_b = 1.0$ (—), 2.0 (—), 3.0 (—), 4.0 (—) and 5.0 (—), respectively.

For the pure SS mode, the magnitudes of all perturbed properties, except $\hat{p}$, are prominently significant in the central region ($z \in [-2, 2]$) where the shear of the base flow velocity (Eq.(1)) varies effectively. Though the pure RB mode may also incite limited perturbations of velocity (Fig. 6(a), (e) and Fig. 7(a), (e)) and vorticity (Fig. 6(b) and Fig. 7(b)) in the central stable stratified layer, it is insufficient to develop the shear instability mode. The other prominent distinction is the profile of $\hat{p}$ (Fig. 6(c) and Fig. 7(c)). Only for the pure SS mode (dashed line), the gradient $\partial\hat{p}/\partial z$ is significant in the central region, while for the pure RB mode, there is generally little variations of $\partial\hat{p}/\partial z$ in the central region. As the shear instability is inherently provoked by the pressure perturbations, the significant variations of other perturbed properties in the central region, are likewise associated with the pure SS mode only.

On the other hand, the pure RB mode exclusively produces remarkable peak structures of $\hat{b}$, $\hat{w}$ and $\hat{b}\hat{w}$ near the interface (around $z = -2$ as $L_b = 3$ designated in this study) between the stable and unstable stratification layers, as shown in Fig. 6(d)-(f) and Fig. 7(d)-(f). In addition to $\tilde{\alpha} = 0.1$ and 0.46 shown here, such 'interface peak' structures are also observed in other $\tilde{\alpha}$ values, thus featuring the eigenfunctions of the pure RB mode. Furthermore, when $\tilde{\alpha}$ increases, the magnitudes of the 'interface peak' structures of $\hat{b}$, $\hat{w}$ and $\hat{b}\hat{w}$ significantly increase from $\tilde{\alpha} = 0.1$ to 0.46 when Fig. 6(d)-(f) and Fig. 7(d)-(f) are compared. The similar enhancements of the 'interface peak' structures with increased $\tilde{\alpha}$ are also found in the range of $\tilde{\alpha} \leq 1$ interested in this paper besides $\tilde{\alpha} = 0.1$ to 0.46 shown here. The growing magnitudes of the 'interface peak' structures associated with the pure RB mode could be attributed to the stability boundary of the pure RB mode shown in Fig. 3. On the stability boundary, the critical J_b decreases with increasing $\tilde{\alpha}$, indicating that the pure RB mode could be easily developed when $\tilde{\alpha}$ increases. Therefore, the magnitudes of $\hat{w}$ and $\hat{b}\hat{w}$ for the pure RB mode also increase with increased $\tilde{\alpha}$.

Overall, Figs. 6 and 7 offer two important implications for the hybrid modes in the SCBL flow. Firstly, the dominant eigenfunctions of the pure RB and SS modes always occur at the established positions, *i.e.*, the symmetric eigenfunctions of the pure SS mode always occur and dominate in the central regions, while the significant 'interface peak' structures of $\hat{b}$, $\hat{w}$ and $\hat{b}\hat{w}$ always accompany the pure RB mode near the interface. Secondly, the established positions of the eigenfunctions for the pure RB and SS modes are also closely associated with the propagative ($\mathrm{Im}[\tilde{\sigma}]$ is significant) and stationary ($\mathrm{Im}[\tilde{\sigma}]$ is insignificant)

feature of previous eigenvalue problems. Physically, as the uprising buoyancy in the pure RB mode inherently 'propagates' upward, its $\mathrm{Im}[\tilde{\sigma}]$ is therefore always significant. On the other hand, the full-grown shear stratified instability, *e.g.*, the Kelvin-Helmholtz mode, develops relatively 'stationary' to the base sheared flow, given negligible $\mathrm{Im}[\tilde{\sigma}]_{\mathrm{SS}}$ all the time.

The two implications elaborated above could help the understandings of how the shear and thermal instabilities contribute to the hybrid features of the SCBL flow. Firstly, as the positions of eigenfunctions for the shear and thermal instabilities are established, whether the shear and thermal instabilities are fully developed or suppressed in the SCBL flow could therefore be evaluated, by comparing the eigenfunctions of the hybrid modes to those of the pure RB and SS modes. Secondly, the eigenfunctions near the interface are always associated with the uprising buoyancy and therefore are also related to the propagative features ($\mathrm{Im}[\tilde{\sigma}]$ is not negligible). With such strong associations, the variations of eigenfunctions near the interface could provides certain insights to explain the results of $\mathrm{Im}[\tilde{\sigma}]_{\mathrm{HRB}}$ and $\mathrm{Im}[\tilde{\sigma}]_{\mathrm{HSS}}$ in Fig. 4.

Figures 8 and 9 show a set of eigenfunctions corresponding to the HRB and HSS mode at $\tilde{\alpha} = 0.1$ and $\tilde{\alpha} = 0.46$, respectively, with a series of J_b near $J_{b,cr}$ and $J_s = 0.1$. Similar results are also found at other $\tilde{\alpha}$ values in Regions I and II. For reference, $J_{b,cr}$ (defined in Fig. 4) at $\tilde{\alpha} = 0.1$ and 0.46 are about 9 and 4, respectively, so that the eigenfunctions plotted by (—), (—) and (—) in Figs. 8 and 9 denote the results when $J_b < J_{b,cr}$ while the eigenfunctions plotted by (—) and (—) in each figure denote the results when $J_b \geq J_{b,cr}$. Because it is found that the HRB and HSS modes always share the eigenfunctions of $\hat{u}$, $\hat{\omega}_y$ and $\hat{p}$ but only distinguish themselves by the eigenfunctions of $\hat{b}$, $\hat{w}$ and $\hat{b}\hat{w}$, the eigenfunctions of both hybrid modes are plotted together in Figs. 8 and 9, respectively, with the subfigures (a)-(f) refer to those of the HSS mode and the subfigures (d)-(i) refer to those of the HRB mode, respectively.

From these two figures, it can be found that both the HRB and HSS modes involve the eigenfunctions near the interface and in the central region, indicating that the thermal and shear stratified instabilities indeed coexist with each other. Hence, the hybrid features of the instabilities in the SCBL flow, as suggested at the beginning of Section IV, are therefore validated. In addition to the common hybrid features, the major results regarding the eigenfunctions of the HRB and HSS mode are summarized as follows.

(a) In the HSS mode, the shear stratified instability is completely developed when

Accepted to Phys. Fluids 10.1063/5.0123044

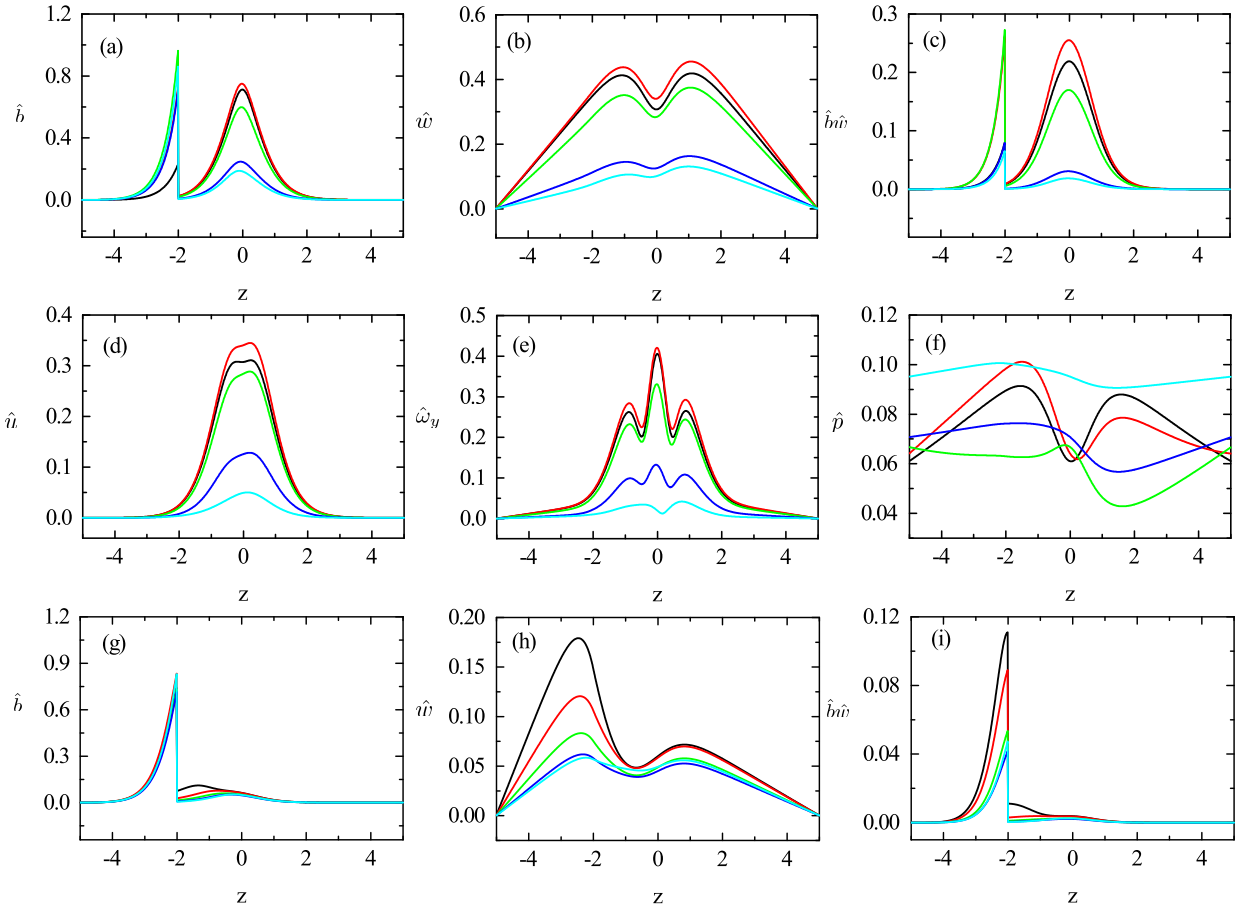

FIG. 8. The profiles of the absolute values of (a) $\hat{b}$, (b) $\hat{w}$, (c) $\hat{b}\hat{w}$, (d) $\hat{u}$, (e) $\hat{\omega}_y$, (f) $\hat{p}$ for the HSS mode, and (g) $\hat{b}$, (h) $\hat{w}$, (i) $\hat{b}\hat{w}$ for the HRB mode in the z direction for a series of J_b at $\tilde{\alpha} = 0.1$ and $J_s = 0.1$ with $J_{b,cr} \approx 9.0$. (—), (—), (—), (—) and (—) denote the profiles at $J_b = 1.0$, 3.0, 5.0, 9.0 and 15.0, respectively.

$J_b < J_{b,cr}$ (denoted by (—), (—) and (—) in Fig. 8(a)-(f) and Fig. 9(a)-(f)), as in the central region all eigenfunctions exhibit almost symmetric peak structures. The symmetric eigenfunctions observed are highly similar to those of the pure SS mode as shown in Fig. 7. As the symmetric features of the pure shear stratified instability are well inherited, the shear stratified instability can be considered as 'fully developed' in the HSS mode. Such 'fully' developed shear instabilities at $J_b < J_{b,cr}$ for the HSS mode provide some insights into the potential appearances of the coherent structures. Similarly, the almost symmetrical eigenfunction structures in the HSS mode may indicate large scale eddy structures, *e.g.*, the Kelvin-Helmholtz eddies, like the pure shear stratified instability. Yet, at the interface both $\hat{b}$ and $\hat{b}\hat{w}$, which are indications of thermal instability, also coexist with their counterparts

Accepted to Phys. Fluids 10.1063/5.0123044

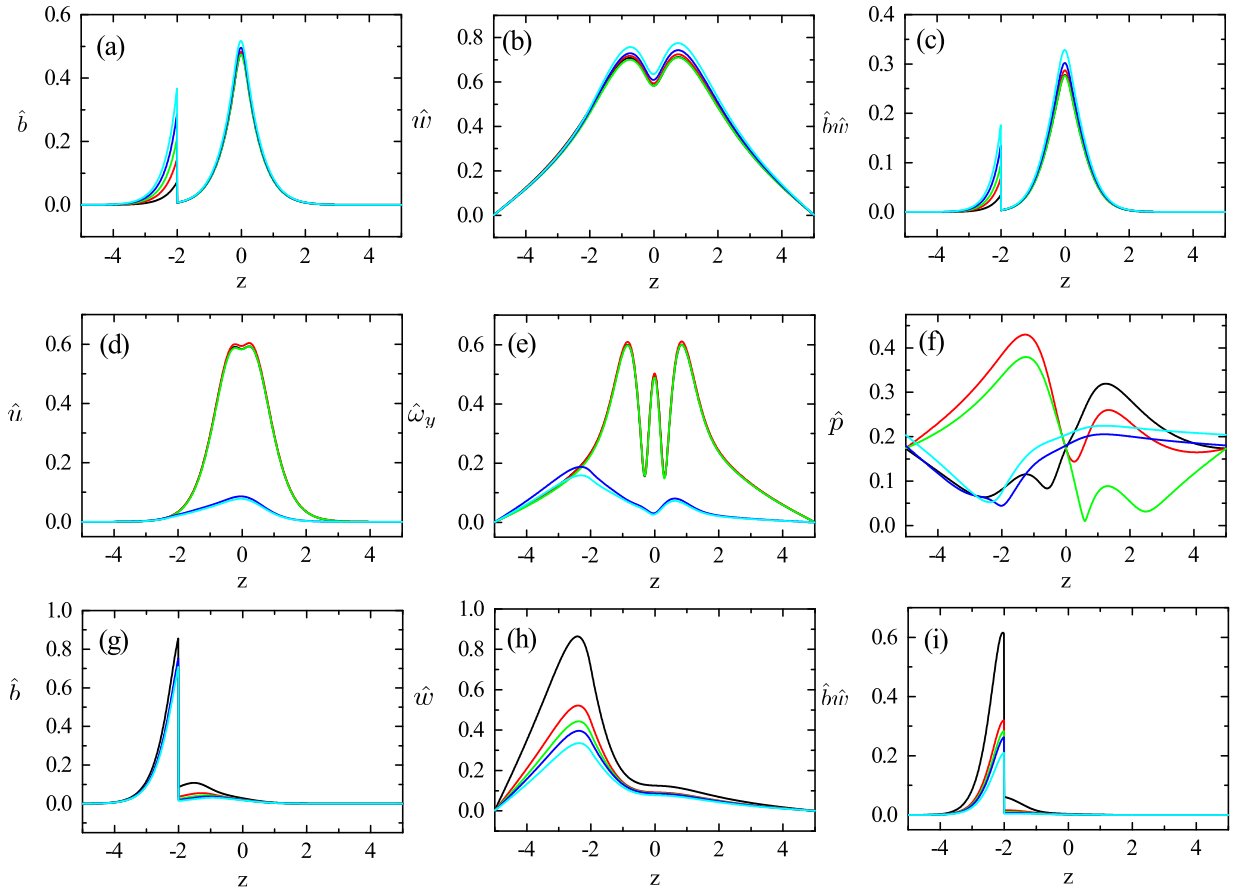

FIG. 9. The profiles of the absolute values of (a) $\hat{b}$, (b) $\hat{w}$, (c) $\hat{b}\hat{w}$, (d) $\hat{u}$, (e) $\hat{\omega}_y$, (f) $\hat{p}$ for the HSS mode, and (g) $\hat{b}$, (h) $\hat{w}$, (i) $\hat{b}\hat{w}$ for the HRB mode in the z direction for a series of J_b at $\tilde{\alpha} = 0.46$ and $J_s = 0.1$ with $J_{b,cr} \approx 4.0$. (—), (—), (—), (—) and (—) denote the profiles at $J_b = 1.0$, 2.0, 3.0, 4.0 and 5.0, respectively.

in the central region. Thus, it is expected that the typical structures of thermal instability, *e.g.*, thermal plumes, may also appear in the HSS mode. Nevertheless, the thermal instability may not develop the large scale RB rolls in the HSS mode. Comparing $\hat{w}$ in the HSS mode (Figs. 8(b) and 9(b)) and those of the pure RB mode (Figs. 6(b) and 7(b)), the peak structures of $\hat{w}$ for the HSS mode are almost symmetrical and occur above the interface where $z = -2$, unlike those of the pure RB mode whose eigenfunctions mainly occur near and below the interface (at about $z \in [-4, -2]$). That is to say, the thermal instability within the HSS mode fails to produce sufficient vertical momentum under the suppression from the developed KH eddy structures. As the large scale RB rolls must involve noticeable perturbations of the vertical momentum near the interface, as shown in Figs. 6(e) and 7(e),

the RB rolls are not developed in the HSS mode. Accordingly, it is suggested that the large scale eddy structures are developed but under the constant penetration and entrainment from the uprising thermal flux or plumes, while the thermal instability is so weak that the thermal flux or plumes are unable to destroy the KH eddies and form the large scale RB rolls.

(b1) In the HRB mode, the shear instability is always 'partly developed' when $J_b < J_{b,cr}$. As denoted by (—), (—) and (—) in Fig. 8(g)-(i) and Fig. 9(g)-(i), the central peak structures of $\hat{b}$ and $\hat{b}\hat{w}$ are not found at all in the HRB mode. The eigenfunctions of $\hat{w}$ are negligible in terms of their magnitudes in the central region in Region II (Fig. 9(h)) either. In Region I (Fig. 8(h)), the eigenfunctions of $\hat{w}$ appear rather weak compared to those near the interface, and overall look very similar to those belong to the pure RB mode shown in Fig. 6(e). Therefore, the absence of the central peak structures of $\hat{b}$, $\hat{w}$ and $\hat{b}\hat{w}$ suggests that the shear stratified instability in the HRB mode is only 'partly developed' on $\hat{u}$, $\hat{\omega}_y$ and $\hat{p}$ at best. Such 'partly developed' shear stratified instabilities at $J_b < J_{b,cr}$ for the HRB mode also imply potential appearances of the corresponding coherent structures. The absence of $\hat{w}$ in the central regions indicates the lack of the perturbed vertical momentum in the same region for the HRB mode. As large eddy structures must also involve strong vertical momentum, unlike the HSS mode, the shear stratified instability may not develop large scale coherent eddy structures in the HRB mode. Such 'partly developed' shear stratified instability allows the uprising thermal flux to easily penetrate through the central region and most likely creates the coherent RB rolls. The potential large scale thermally convective structures in the HRB mode are also supported by its propagative features, where $\mathrm{Im}[\tilde{\sigma}]_{\mathrm{HRB}}$ is always significant. Though in the present linear analysis, the coherent structures associated with 'partly developed' shear instability are unknown via linear analysis, it is suggested that the remaining eigenfunctions of $\hat{u}$, $\hat{\omega}_y$ and $\hat{p}$ in the central region may involve less vigorous vorticity structures, *e.g.*, the periodic overturning wave or the patch of local turbulence usually observed in atmospheric and oceanic flow. These less vigorous vorticity structures may still modify the influences of the convective rolls on the interface dynamics.

(b2) In the HRB mode, the shear instability is 'undeveloped' when $J_b \geq J_{b,cr}$ (denoted by (—) and (—) in Fig. 8(g)-(i) and Fig. 9(g)-(i)), as all eigenfunctions are of insignificant magnitudes in the central region, especially for $\hat{b}$, $\hat{w}$ and $\hat{b}\hat{w}$. In contrast, these eigenfunctions at $J_b \geq J_{b,cr}$ are analogous to those of the pure RB mode shown in Fig. 6(g)-(i) and

Fig. 7(g)-(i), indicating that the HRB mode may gradually approach the pure RB mode once $J_b \geq J_{b,cr}$. Nonetheless, the 'interface peak' structures of $\hat{u}$, $\hat{\omega}_y$ and $\hat{p}$ are still not developed in Region I (Fig. 8), suggesting that the thermal instability is still suppressed by the 'undeveloped' shear instability, even when the unstable stratification becomes conducive to the thermal instability in terms of $J_b > J_{b,cr}$. The other indirect evidence to support this argument is the reduced magnitudes of $\hat{b}$, $\hat{w}$ and $\hat{b}\hat{w}$ in Region I for the HRB mode when $J_b > J_{b,cr}$ (— and —) in Fig. 8(g)-(i)), compared to those of the pure RB mode ((—) and (—) in Fig. 6(g)-(i)). For instance, the magnitudes of the interface peak structure of $\hat{b}$ in Fig. 8(g) are less than 0.9, slightly smaller than those of $\hat{b}$ with magnitudes of 1 in Fig. 6(g). The observation that the 'undeveloped' shear instability could still suppress the thermal instability is very similar to the conclusions from the recent works on the SRBP flow by Fontana *et al.*[4,6]. In their work, even though the non-deformation assumptions are made, the shear is found to contribute significantly to the instability of the flow system. In the present study, the 'undeveloped' shear instability may only induce relatively negligible deformations on the interface compared to the 'fully developed' and 'partly developed' shear instabilities, *e.g.*, KH eddies and periodic waves, thus may be very close to the non-deformation assumptions. If the shear instability could still have certain influences on the overall shear-thermal interactive flow system even under the strict non-deformation assumptions in SRBP flow, likewise, it should also be expected that the 'undeveloped' shear instability in the present study should also modify the thermal instability.

(c) As J_b increases, the uprising buoyancy enhances, so that the shear stratified instabilities in both the HRB and HSS modes decay. The decay of the instabilities is demonstrated with the eigenfunctions of $\hat{u}$, $\hat{\omega}_y$ and $\hat{p}$ in the central region, whose magnitudes decrease with increasing J_b as shown in Fig. 8(d)-(f) and Fig. 9(d)-(f). Nevertheless, the shear instabilities decay in different ways in Regions I and II, which are also closely associated with the variations of $\mathrm{Im}[\tilde{\sigma}]_{\mathrm{HSS}}$ with increased J_b as shown in Fig. 4. The different decay fashions in Regions I and II may also be associated with the 'shear enhancement' and 'shear sheltering' reported in previous studies on the SCBL flow.

(c1) In Region I (Fig. 8(a)-(f)), the shear stratified instability decays thoroughly as J_b increases towards $J_{b,cr}$. When J_b increases to 5.0, the eigenfunctions of $\hat{p}$ vary little near the interface (— in Fig. 8(f)), indicating that the shear instability loses its influence near the interface. As a result, $\hat{b}$ near the interface immediately boosts (— in Fig. 8(a)) and also

leads to the boost of $\hat{b}\hat{w}$ near the interface (— in Fig. 8(c)). As it is difficult to identify the 'interface peak' at $J_b = 3.0$ (—) in Fig. 8(a) and (c), it should be mentioned that the 'interface peak' at $J_b = 3.0$ (—) overlaps with those at $J_b = 1.0$ (—) in the two figures. Once J_b exceeds $J_{b,cr}$, as denoted by (—) and (—), the gradients of the pressure perturbation $\partial\hat{p}/\partial z$ are further compromised (Fig. 8(f)), so that the magnitudes of the central peak structures for the rest eigenfunctions are also significantly weakened (Fig. 8(a)-(e)). Due to such an overall decay, the 'interface peaks' of $\hat{b}$ and $\hat{b}\hat{w}$ reversely become comparable to or even dominate over their counterparts in the central region.

The point (c1) well explains the results of $\mathrm{Im}[\tilde{\sigma}]_{\mathrm{HSS}}$ shown in Fig. 4(d). As suggested by the second implication from Figs. 6 and 7, the 'interface peak' structures always correspond to the thermal instability and the associated $\mathrm{Im}[\tilde{\sigma}]$ in the present temporal linear analysis. Therefore, the reversely dominant 'interface peaks' of $\hat{b}$ and $\hat{b}\hat{w}$, caused by the overall declined central peak structures as the consequences of the decayed shear instabilities, strongly indicate that $\mathrm{Im}[\tilde{\sigma}]_{\mathrm{HSS}}$ should become significant near $J_{b,cr}$. The significant $\mathrm{Im}[\tilde{\sigma}]_{\mathrm{HSS}}$ is indeed found in Fig. 4(d).

It should also be noted that the boosted 'interface peak' of $\hat{b}\hat{w}$ at $J_b = 5.0$ (— in Figure 8(c)) has its magnitude of about 0.3 almost three times of that in the pure RB mode (Fig. 6(f)), whose magnitudes are all below 0.1. This fact suggests that at certain specific conditions, the presence of shear could potentially prompt the development of thermal instability. This observation reminds us of one case frequently reported on previous field observations and numerical simulations on the SCBL (as reviewed in[9]), where the imposed wind shear is found to enhance the overall entrainment.

In addition, the point (c1) implicates that the decay of the shear instability also leads to the similar appearances of the eigenfunctions between the HSS and HRB modes, especially for those near the interface as denoted by (—) and (—) in Fig. 8(a)-(f). Such similar appearances of the eigenfunctions also agree with the merging tendency between $\mathrm{Im}[\tilde{\sigma}]_{\mathrm{HSS}}$ and $\mathrm{Im}[\tilde{\sigma}]_{\mathrm{HRB}}$ as also shown in Fig. 4(d). Moreover, the magnitudes of $\hat{b}\hat{w}$ when $J_b > J_{b,cr}$ (—, —) for the HSS mode (Fig. 8(c)), the HRB mode (Fig. 8(f)) and the pure RB mode (Fig. 6(f)) are all around 0.06, indicating that the shear instability no longer has a primary influence on the entrainment, though its secondary role may still modify the thermal instability as suggested by point (b) above.

(c2) In Region II (Fig. 9(a)-(f)), the shear stratified instability seems more robust, in that

the symmetrical eigenfunctions of $\hat{b}$, $\hat{w}$, $\hat{b}\hat{w}$ sustain when J_b approaches and exceeds $J_{b,cr}$, even though $\hat{u}$, $\hat{\omega}_y$ and especially $\hat{p}$ decay significantly in the central region during the transition. Meanwhile, the 'interface peak' structures of $\hat{b}$ and $\hat{b}\hat{w}$ are always subdued to their robust counterparts in the central regions. This is closely associated with the sustained stationary feature of the HSS mode as shown in Fig. 4(c). Because of the robust eigenfunctions of $\hat{b}\hat{w}$ in the central region, the 'interface peak' structures are still overwhelmed. As suggested by the second implications from Figs. 6 and 7, the overwhelmed $\hat{b}\hat{w}$ near the interface would still provide insignificant $\mathrm{Im}[\tilde{\sigma}]$, which agrees well with negligible $\mathrm{Im}[\tilde{\sigma}]_{\mathrm{HSS}}$ shown in Fig. 4(c).

While comparing the magnitudes of the 'interface peaks' of $\hat{b}$ and $\hat{b}\hat{w}$ for the HSS mode (Fig. 9(a) and (c)) and the pure RB mode (Fig. 7(d) and (f)) in Region II, it is found that the 'interface peaks' are in fact suppressed by the shear instability, as the maximum magnitudes of the 'interface peaks' $\hat{b}\hat{w}$ are below 0.2 for the HSS mode (except for $J_b = 1.0$) and all above 0.2 for the pure RB mode. Thus, the influence of the shear instability in Region II is quite opposite to what is found in Region I as mentioned in point (c1) above. This fact implicates 'shear sheltering' suggested by the previous studies on the SCBL flow[48–50]. The 'shear sheltering' could be attributed to the robust of shear instability, in which the coherent large vortex structures are very likely to be developed and suppress the formation of convective rolls as also discussed in point (a). Under such a circumstance, the entrainment of buoyancy flux could only be achieved via the uprising thermal plumes or flux, which, apparently, supplies much less buoyancy flux compared to the significant vertical momentum from the convective rolls in the pure RB mode.

V. DISCUSSION AND CONCLUSION

As proposed at the beginning of Section IV, in the SCBL flow the shear stratified and thermal instabilities always coexist, therefore leading to the essentially hybrid features between the two fundamental instabilities. Such hybrid features have been validated by the presences of the HRB and HSS modes and elaborated by their corresponding eigenfunctions which occurs both near the interface layer and inside the central shear stratified layer. The interactions between the HRB and HSS modes create highly dynamical characteristics of the SCBL flow, which is well represented by the critical boundary defined by the critical unstable stratification factor $J_{b,cr}$ as shown Fig. 4. It is found that the critical boundary

depends not only on the unstable and stable stratifications in terms of J_b and J_s, but also on the wavenumbers of the imposed perturbations distinguished with two distinct regions.

The complex dynamics of the SCBL flow are further illustrated by the subordinate eigenfunctions of the HRB and HSS modes in Regions I and II, respectively. The 'well-developed' shear instabilities, in which the vortex structures created by the shear are physically expected, distinguish the HSS mode from the HRB mode. When J_b increases, different transitional behaviors of the HSS mode in Regions I and II further complicate the dynamics. For the HSS mode in Region I, the shear instabilities gradually decay as J_b increases, reversely make the 'interface peak' of $\hat{b}\hat{w}$ become comparable and even dominant, which corresponds to the propagative feature (Im$[\tilde{\sigma}]$ is significant). Particularly, when J_b is slightly smaller than $J_{b,cr}$, the 'interface peak' of $\hat{b}\hat{w}$ is significantly boostes compared to that of the pure RB mode with the same wavenumber, indicating the 'shear enhancement' also frequently reported in previous observations on the SCBL flow. For the HSS mode in Region II, nevertheless, the shear instability is robust to the enhanced unstable stratification, therefore leading to the corresponding stationary feature (Im$[\tilde{\sigma}]$ is negligible) and the decline of the 'interface peak' of $\hat{b}\hat{w}$ compared to that of the pure RB mode with the same wavenumber. Such a decline implicates the 'shear sheltering' reported in previous studies on the SCBL flow. For the HRB mode, the shear instability is 'partly developed' when $J_b < J_{b,cr}$ and 'undeveloped' when $J_b > J_{b,cr}$. Though the expected convective rolls dominate in the HRB mode and sustain the propagative feature as shown in Fig. 4, while comparing the eigenfunctions in the HRB mode with those in the pure RB mode it is still found that the 'partly developed' and the 'undeveloped' shear instabilities still suppress the further development of thermal instability, which agrees with previous observations that the convective boundary layer is indeed modified by the wind shear as reported in previous studies on the SCBL flow.

As the majority of the previous studies on the SCBL flow have focused on the scenarios with strong thermal convection, *e.g.*, cloud-free or the daytime atmospherical boundary layers, the HRB mode is often observed and reported, with the prevalence of the well developed thermal instability and the associated convective roll structures. The shear instability in the HRB mode seems only play a secondary role as it only modifies the convective rolls near the interface or in the entrainment zone. Nevertheless, the unique feature of the SCBL flow is the additional HSS mode, in which the shear instability is decisive as it is able to produce significant vortex structures comparable to those of the convective rolls. As described and

discussed by the points (a) and (c) of the eigenfunction section, the different transitional behaviors of the HSS mode in Regions I and II are closely related with the 'shear enhancement' and 'shear sheltering' reported from previous studies on the SCBL flow. Thus, it is suggested that the 'shear enhancement' and 'shear sheltering' are not contradictory with each other, in fact they just involve the different behaviors of the HSS mode.

Moreover, as reviewed in Section I, the concept of the HSS mode of the SCBL flow is not limited to the strong thermal convection, which is predominant in the majority of studies on the SCBL flow topic. When the thermal convection is moderate or even weak, the HSS mode is highly expected and may even prevail. For instance, during evening time, moderate or weak thermal convection could be produced by other on-ground heat sources, such as the urban and industrial regions, and if the wind shear is sufficient, the HSS mode and its potential vortex structure interactions between the shear and thermal instabilities are highly possible to occur. Under cloudy (weak thermal convective condition) and windy (strong wind shear) weathers, the HSS mode may also prevail in the SCBL flow. Thus, the hydrodynamics of the HSS mode obtained in the present study may also play a key role to understand the relevant heat and mass transfer in these SCBL flows with moderate or weak thermal convection.

In addition to geophysical circumstances, the SCBL flow including the HSS and HRB modes may also potentially occur when the shear instability is induced by unbounded flow, *e.g.*, the mixed layer and the related Kelvin-Helmholtz instability, the jet flow and its associated wake, *etc.*. If the significant vortex structures produced by these unbounded flows interact with the thermally convective flux or structures, the similar interactive dynamics, where the shear instability has more active influences on or even suppresses the thermal instability, may also potentially appear as what were shown in this study.

ACKNOWLEDGMENTS

The support from the Jiangxi Provincial Natural Science Foundation (Grant No. 20212BAB214011) and the early career development program of China East Jiaotong University (Grant No. 10032003419068) is gratefully acknowledged.

DECLARATIONS OF COMPETING INTEREST

The authors declare that they have no conflicts of interest to disclose.

APPENDIX

Appendix A

Both the basic flow and the total flow (basic flow + infinitesimal perturbations) are governed by the equations (5)-(7), *i.e.*,

$$\nabla \cdot \mathbf{U} = 0, \tag{A1}$$

$$\bar{\theta}\frac{\partial \mathbf{U}}{\partial t} + \bar{\theta}\mathbf{U} \cdot \nabla \mathbf{U} = -\nabla P(z) - \frac{[\theta_b(z) - \bar{\theta}]}{Fr^2}\vec{k}, \tag{A2}$$

$$\frac{\partial \theta_b(z)}{\partial t} + \mathbf{U} \cdot \nabla \theta_b(z) = 0, \tag{A3}$$

and

$$\nabla \cdot (\mathbf{U} + \mathbf{u}') = 0, \tag{A4}$$

$$\bar{\theta}\frac{\partial (\mathbf{U} + \mathbf{u}')}{\partial t} + \bar{\theta}(\mathbf{U} + \mathbf{u}') \cdot \nabla (\mathbf{U} + \mathbf{u}') = -\nabla [P(z) + p'] - \frac{[\theta_b(z) + \theta' - \bar{\theta}]}{Fr^2}\vec{k}, \tag{A5}$$

$$\frac{\partial [\theta_b(z) + \theta']}{\partial t} + (\mathbf{U} + \mathbf{u}') \cdot \nabla [\theta_b(z) + \theta'] = 0. \tag{A6}$$

Therefore, by subtracting the equations for the basic flow, *i.e.*, Eqs. (A1)-(A3), from the corresponding equations for the total flow, *i.e.*, Eqs. (A4)-(A6), and assuming the product of an infinitesimal quantity and its gradient is negligible[35], *i.e.*, $\mathbf{u}' \cdot \nabla \mathbf{u}' \approx 0$ and $\mathbf{u}' \cdot \nabla \theta' \approx 0$, the following perturbation equations are deduced,

$$\nabla \cdot \mathbf{u}' = 0, \tag{A7}$$

$$\bar{\theta}\frac{\partial \mathbf{u}'}{\partial t} + \bar{\theta}(\mathbf{U} \cdot \nabla \mathbf{u}' + \mathbf{u}' \cdot \nabla \mathbf{U}) = -\nabla p' - \frac{\theta'}{Fr^2}\vec{k}, \tag{A8}$$

$$\frac{\partial \theta'}{\partial t} + \mathbf{U} \cdot \nabla \theta' + \mathbf{u}' \cdot \nabla \theta_b(z) = 0. \tag{A9}$$

For the sheared stratified flows considered in this paper, the base flow is assumed to be in the x-direction and to vary with the vertical coordinate z only, *i.e.*,

$$\mathbf{U}(z) = U(z)\vec{i}. \tag{A10}$$

With this, the dot product terms in Eq. (A8) and Eq. (A9) become,

$$\mathbf{U} \cdot \nabla \mathbf{u}' = U(z)\frac{\partial u'}{\partial x}\vec{i} + U(z)\frac{\partial v'}{\partial x}\vec{j} + U(z)\frac{\partial w'}{\partial x}\vec{k},$$

$$\mathbf{u}' \cdot \nabla \mathbf{U} = w' \frac{\partial U(z)}{\partial z} \vec{i}, \quad \mathbf{U} \cdot \nabla \theta' = U(z) \frac{\partial \theta'}{\partial x}, \quad \mathbf{u}' \cdot \nabla \theta_b(z) = w' \frac{\partial \theta_b(z)}{\partial z}.$$

These lead to the following perturbation equations,

$$\frac{\partial u'}{\partial x} + \frac{\partial v'}{\partial y} + \frac{\partial w'}{\partial z} = 0, \tag{A11}$$

$$\bar{\theta} \frac{\partial u'}{\partial t} + \bar{\theta} U(z) \frac{\partial u'}{\partial x} + \bar{\theta} w' \frac{\partial U(z)}{\partial z} = -\frac{\partial p'}{\partial x}, \tag{A12}$$

$$\bar{\theta} \frac{\partial v'}{\partial t} + \bar{\theta} U(z) \frac{\partial v'}{\partial x} = -\frac{\partial p'}{\partial y}, \tag{A13}$$

$$\bar{\theta} \frac{\partial w'}{\partial t} + \bar{\theta} U(z) \frac{\partial w'}{\partial x} = -\frac{\partial p'}{\partial z} - \frac{\theta'}{Fr^2}, \tag{A14}$$

$$\frac{\partial \theta'}{\partial t} + U(z) \frac{\partial \theta'}{\partial x} + w' \frac{\partial \theta_b(z)}{\partial z} = 0. \tag{A15}$$

Appendix B

If the following relations are defined,

$$\tilde{\alpha} = (\alpha^2 + \beta^2)^{1/2}, \quad \tilde{p} = \frac{\tilde{\alpha}}{\alpha} \hat{p}, \quad \tilde{u} = \frac{\alpha \hat{u} + \beta \hat{v}}{\tilde{\alpha}}, \quad \tilde{\theta} = \frac{\tilde{\alpha}}{\alpha} \hat{\theta}, \tag{B1}$$

where the tilde symbol ('~') denotes the Squire transformation properties, then the operation of $[\alpha\times$ Eq. (21) $+ \beta\times$ Eq. (22)$]/\alpha$ will lead to,

$$\tilde{\alpha}(iU + \frac{\sigma}{\alpha})\tilde{u} + U_z \tilde{w} = -i\tilde{\alpha}\frac{\tilde{p}}{\bar{\theta}} \tag{B2}$$

The differentiation with respect to z of the above equation results in,

$$i\tilde{\alpha} U_z \tilde{u} + i\tilde{\alpha} U D\tilde{u} + \frac{\tilde{\alpha}\sigma}{\alpha} D\tilde{u} + (U_{zz} + U_z D)\hat{w} = -i\frac{\tilde{\alpha}}{\bar{\theta}} D\tilde{p}, \tag{B3}$$

where the subscript 'zz' denotes the second order differentiation with respect to z.

Putting the above relation $\tilde{u} = (\alpha\hat{u} + \beta\hat{v})/\tilde{\alpha}$ into the continuity equation (20) gives the following equation,

$$i\tilde{\alpha}\tilde{u} = -D\hat{w}, \tag{B4}$$

and a further differentiation with respect to z of this equation leads to,

$$D\tilde{u} = -\frac{D^2\hat{w}}{i\tilde{\alpha}}. \tag{B5}$$

With Eq. (B4) and Eq. (B5), Eq. (B3) changes to,

$$i\frac{\sigma}{\alpha}D^2\hat{w} - UD^2\hat{w} + U_{zz}\hat{w} = -i\frac{\tilde{\alpha}}{\bar{\theta}}D\tilde{p}. \tag{B6}$$

The product of $(\tilde{\alpha}/\alpha)$ and Eq. (23) is then,

$$\tilde{\alpha}(iU + \frac{\sigma}{\alpha})\hat{w} = -\frac{1}{\bar{\theta}}D\tilde{p}, \tag{B7}$$

and the product of $i\tilde{\alpha}$ and the above equation is,

$$-\tilde{\alpha}^2(U - i\frac{\sigma}{\alpha})\hat{w} = -i\frac{\tilde{\alpha}}{\bar{\theta}}D\tilde{p}. \tag{B8}$$

Substracting Eq. (B6) from Eq. (B8) and then multiplying by $(-i)$ give

$$\tilde{\sigma}\hat{w} = -i\tilde{\alpha}(U\nabla_s^2 - U_{zz}\hat{w} \tag{B9}$$

where $\tilde{\sigma} = \sigma\tilde{\alpha}/\alpha$ is the Squire temporal growth rate of the perturbations properties and the Squire Laplacian operator ∇_s^2 is defined as $\nabla_s^2 = D^2 - \tilde{\alpha}^2$.

The product of $\tilde{\alpha}/\alpha^2$ and Eq. (24) is

$$\frac{\sigma}{\alpha}\tilde{\theta} = -\frac{\tilde{\alpha}}{\alpha^2}\theta_{b,z}\hat{w} - iU\tilde{\theta}. \tag{B10}$$

Multiplying Eq. (B9) and Eq. (B10) by $\tilde{\alpha}$ and then writing them in matrix form gives,

$$\tilde{\sigma}\begin{bmatrix} \nabla_s^2 & \\ & I \end{bmatrix}\begin{bmatrix} \hat{w} \\ \tilde{\theta} \end{bmatrix} = \begin{bmatrix} -i\tilde{\alpha}(U\nabla_s^2 - U_{zz}) & \dfrac{\tilde{\alpha}^2}{\bar{\theta}Fr^2} \\ -\tilde{\theta}_{b,z} & -i\tilde{\alpha}U \end{bmatrix}\begin{bmatrix} \hat{w} \\ \tilde{\theta} \end{bmatrix}, \tag{B11}$$

where $\tilde{\sigma} = \sigma\tilde{\alpha}/\alpha$ is the Squire temporal growth rate of the perturbations properties and $\tilde{\theta}_{b,z} = \theta_{b,z}\tilde{\alpha}^2/\alpha^2$ is the Squire temperature gradient.

Appendix C

To test the influence of L_b, the over length of the bottom domain $L + L_b$, as shown in FIG. 1, is fixed at 5, which is five times of the characteristic length scale $L_c = 1$ as suggested in Section II. Based on the fixed $L + L_b = 5$, L_b is gradually increased towards the central line of the sheared stratified layer ($z = 0$), so that the proportion $L_b/(L + L_b)$ also increases. If L_b increases beyond a certain extent, the $\theta = tanh(z)$ profile will be cutoff due to the insufficient length scale L. To ensure the integrity of the $\theta = tanh(z)$ profile in the central sheared stratified layer, L_b must be setup below such upper limit.

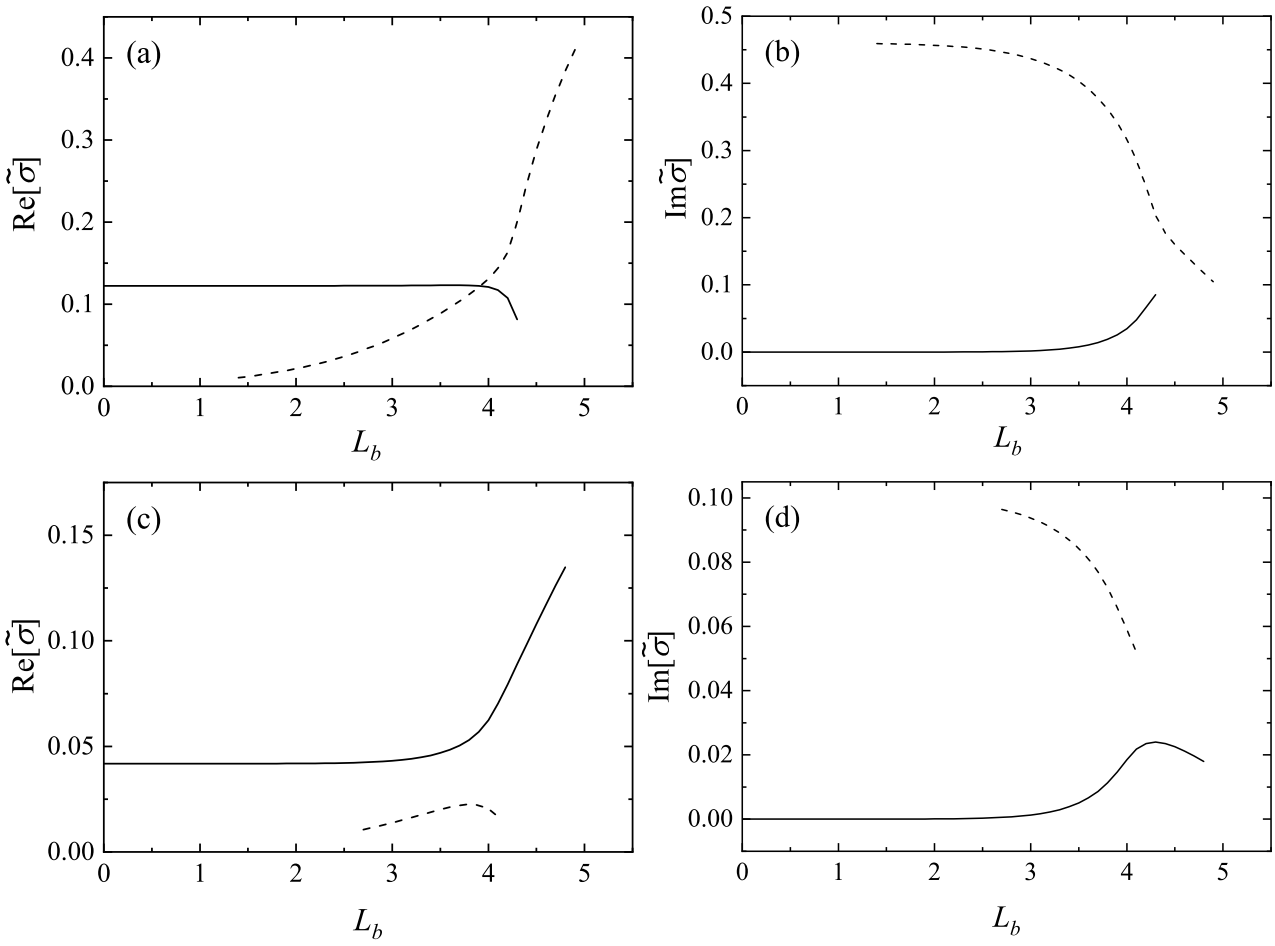

FIG. 10. The real and imaginary parts of $\tilde{\sigma}$ plotted against L_b at $\tilde{\alpha} = 0.46$ ((a) and (c)) and at $\tilde{\alpha} = 0.1$ ((b) and (d)) with $J_s = 0.1$ and $J_b = 1.0$. The solution of the HSS and HRB modes are denoted by the solid and dashed lines, respectively.

Figure 10 shows the real and imaginary parts of $\tilde{\sigma}$ plotted against L_b at $\tilde{\alpha} = 0.46$ (FIG. 10(a) and (b)) and $\tilde{\alpha} = 0.1$ (FIG. 10(c) and (d)), respectively, with fixed $J_s = 0.1$ and $J_b = 1.0$. $\tilde{\alpha} = 0.1$ and 0.46 are two typical wavenumbers in Regions I and II defined in FIG. 3 in Section IV. It is found that the results of Re$[\tilde{\sigma}]$ and Im$[\tilde{\sigma}]$ at other $\tilde{\alpha}$, $J_s < J_{s,cr} = 0.25$ and $J_b > J_{b,cr}$ values in Regions I and II are similar to those at $\tilde{\alpha} = 0.1$ and 0.46, thus they are not presented here.

For the HSS mode (the solid lines) at both $\tilde{\alpha} = 0.1$ and 0.46, Re$[\tilde{\sigma}]$ and Im$[\tilde{\sigma}]$ exhibit their dependencies on L_b at about $L_b > 3$. Such dependencies confirm the upper limit of L_b; above which the bottom unstable stratification begins to compromise the central stable

stratifications. Thus, to ensure the occurrence of the shear instability from the base flow profile, L_b must be setup below such upper limit at $L_b = 3$. On the other hand, for the HRB mode at $\tilde{\alpha} = 0.1$ (the dashed line in FIG. 10(c) and (d)), both its Re$[\tilde{\sigma}]$ and Im$[\tilde{\sigma}]$ only appear from about $L_b > 2.6$, suggesting that there is a lower limit of L_b, above which the HRB mode could exist. Together with the lower and upper limits of L_b, it is suggested that L_b fixed at 3, where both the HSS and HRB modes would develop without the influences from L_b, is appropriate.

Physically, $L_b = 3$ is also appropriate. First, in a real SCBL flow, the inherent unstable thermal convection would quickly occupy the domain below the central sheared stratified layer, therefore $L_b = 3$ also approximates the real circumstance. Although in a real SCBL flow the thermal convection could quickly overcome the central sheared stratified layer, such dynamics occurs only after the shear and thermal instabilities are developing. Therefore the setup of $L_b = 3$ also keeps the integrity of the base flow to ensure the occurrence of both the shear and thermal instabilities.

REFERENCES

[1]R. E. Kelly, "The onset and development of thermal convection in fully developed shear flows," Adv. Appl. Mech. **31**, 35-112 (1994).

[2]X. Nicolas, "Bibliographical review on the Poiseuille–Rayleigh–Bénard flows: the mixed convection flows in horizontal rectangular ducts heated from below," Int. J. Thermal Sci. **41**, 961-1016 (2002).

[3]X. Nicolas, N. Zoueidi, S. Xin, "Influence of a white noise at channel inlet on the parallel and wavy convective instabilities of Poiseuille-Rayleigh-Bénard flows," Phys. Fluids **24**, 084101 (2012).

[4]E. Fontana, E. Mancusi, A. A. U. de Souza, S. M. A. G. U. de Souza, "Stability analysis of stratified Rayleigh-Bénard-Poiseuille convection: influence of the shear flow," Chem. Eng. Sci. **126**, 67–79 (2015).

[5]E. Fontana, E. Mancusi, A. A. U. de Souza, S. M. A. G. U. de Souza, "Stability analysis of stratified Rayleigh-Bénard-Poiseuille convection. Part II: Influence of thermocapillary forces," Chem. Eng. Sci. **155**, 99–110 (2016).

[6]E. Fontana, E. Mancusi, A. A. U. de Souza, S. M. A. G. U. de Souza, "Stability analysis of

stratified Rayleigh-Bénard-Poiseuille convection. Part III: Interface deformation," Chem. Eng. Sci. **203**, 333-345 (2019).

[7]R. J. Conzemius, E. Fedorovich, "Dynamics of sheared convective boundary layer entrainment. Part I: Methodological background and large-eddy simulations," J. Atmo. Sci. **63**, 1151-1178 (2006).

[8]R. B. Stull, An Introduction to Boundary Layer Meteorology, Kluwer, 1988.

[9]E. Fedorovich, R. Conzemius, "Effects of wind shear on the atmospheric convective boundary layer structure and evolution," Acta Geophysica **56**, 114-141 (2008).

[10]C. Liu, E. Fedorovich, J. Huang, "Revisiting entrainment relationships for shear-free and sheared convective boundary layers through large-eddy simulations," Quart. J. Roy. Meteor. Soc. **144**, 2182–2195 (2018).

[11]T. J. Shay, M. C. Gregg, "Turbulence in an oceanic convective mixed layer," Nature **310**, 282-285 (1984).

[12]T. Endoh, T. Matsuno, Y. Yoshikawa, E. Tsutsumi, "Estimates of the turbulent kinetic energy budget in the oceanic convective boundary layer," J. Oceanogr. **70** 81-90 (2014).

[13]H. Yamazaki, H. Honma, T. Nagai, M. J. Doubell, K. Amakasu, M. Kumagai, "Multilayer biological structure and mixing in the upper water column of Lake Biwa during summer 2008," Limnology **11**, 63-70 (2010).

[14]T. J. Lyons, W. D. Scott, Principles of Air Pollution Meteorology, CRC Press, 1990.

[15]J. R. Garratt, The Atmospheric Boundary Layer, Cambridge University Press, 1992.

[16]J. P. Mellado, "Cloud-top entrainment in stratocumulus clouds," Annu. Rev. Fluid Mech. **49**, 145-169 (2017).

[17]I. Isao, Y. Yukio, "Passive scalar diffusion in and above urban-like roughness under weakly stable and unstable thermal stratification conditions," J. Wind. Eng. Ind. Aerodyn. **148**, 18-33 (2016).

[18]T. Gronemeier, S. Raasch, E. Ng, "Effects of unstable stratification on ventilation in Hong Kong," Atmosphere **8**(9), 168 (2017).

[19]T. Grylls, I. Suter, M. van Reeuwijk, "Steady-state large-eddy simulations of convective and stable urban boundary layers," Bound.-Layer Meteorol. **175**, 309-341 (2020).

[20]F. Tang, L. J. Li, M. S. Dong, Q. Wang, F. Z. Mei, L. H. Hu, "Characterization of buoyant flow stratification behaviors by Richardson (Froude) number in a tunnel fire with complex combination of longitudinal ventilation and ceiling extraction," Appl. Therm. Eng. **110**,

1021-1028 (2017).

[21]S. Gannouni, J. Zinoubi, R. B. Maad, "Numerical study on the thermal buoyant flow stratification in tunnel fires with longitudinal imposed airflow: effect of an upstream blockage," Int. J. Therm. Sci. **136**, 230-242 (2019).

[22]C. Fan, L. Yang, D. Luan, T. Chen, A. Jiao, R. Ouyang, J. Wang, C. Chen, "Experimental study on the effect of canyon cross wind on temperature distribution of buoyancy-induced smoke layer in tunnel fires," Transp. Saf. Environ. **3**(4), tdab023 (2021).

[23]G. Horstmann, N. Weber, T. Weier, "Coupling and stability of interfacial waves in liquid metal batteries," J. Fluid Mech. **845**, 1-135 (2018).

[24]A. Pinarbasi "Interface stabilization in two-layer channel flow by surface heating or cooling," Eur. J. Mech. B Fluids **21**, 225–236 (2002).

[25]J. W. Deardorff, "Prediction of convective mixed-layer entrainment for realistic capping inversion structure," J. Atmo. Sci. **36**, 424-436 (1979).

[26]M. C. van Zanten, P. G. Duynkerke, J. W. M. Cuijpers, "Entrainment parameterization in convective boundary layers," J. Atmo. Sci. **56**, 813-828 (1999).

[27]Michalke, A. "On the inviscid instability of the hyperbolictangent velocity profile. Journal of Fluid Mechanics," J. Fluid Mech. **19**(4), 543-556 (1964).

[28]Michalke, A. "On spatially growing disturbances in an inviscid shear layer," J. Fluid Mech. **23**(3), 521-544 (1965).

[29]Huerre, P., & Monkewitz, P. "Absolute and convective instabilities in free shear layers," J. Fluid Mech. **159**, 151-168 (1985).

[30]Healey, J. "Destabilizing effects of confinement on homogeneous mixing layers," J. Fluid Mech. **623**(3), 241-271 (2009).

[31]Bhardwaj, D.& Guha, A. "Nonlinear modeling of stratified shear instabilities, wave breaking, and wave-topography interactions using vortex method," Phys. Fluid. **30**(1), 10.1063/1.5006654 (2018).

[32]Howland, C., Taylor, J., & Caulfield, C. "Mixing in forced stratified turbulence and its dependence on large-scale forcing," J. Fluid Mech. **898**, A7 (2020).

[33]Caulfield, C "Layering, Instabilities, and Mixing in Turbulent Stratified Flows," Annu. Rev. Fluid Mech. **53**, 113-145 (2021).

[34]Natanael K. "On physical optics approximation of stratified shear flows with eddy viscosity," Phys. Fluid. **33(5)**, 10.1063/5.0048550 (2021).

[35]P. G. Drazin and W. H. Reid, *Hydrodynamic Stability* (second edition) (Cambridge University Press, 2004).

[36]J. A. Whitehead, M. M. Chen, "Thermal instability and convection of a thin fluid layer bounded by a stably stratified region," J. Fluid Mech. **40**(3), 549-576 (1972).

[37]W.-Y. Sun, "Linear stability of penetrative convection," J. Atmo. Sci. **33**, 1911-1920 (1976).

[38]R. Conzemius, E. Fedorovich, "Bulk models of the sheared convective boundary layer: evaluation through large eddy simulations," J. Atmo. Sci. **64**, 786-807 (2007).

[39]D. K. Lilly, "Models of cloud-topped mixed layers under a strong inversion," Quart. J. Roy. Meteor. Soc. **94**(401), 292-309 (1968).

[40]D. Pino, J. V.-G. de Arellano, S.-W. Kim, "Representing sheared convective boundary layer by zeroth- and first-order-jump mixed-layer models: large-eddy simulation verification," J. Appl. Meteorol. Climatol. **45**, 1224-1243 (2006).

[41]D. Pino, J. V.-G. de Arellano, "Effects of shear in the convective boundary layer: analysis of the turbulent kinetic energy budget," Acta Geophysica **56**, 167-193 (2008).

[42]C. Liu, E. Fedorovich, J. Huang, "Revisiting entrainment relationships for shear-free and sheared convective boundary layers through large-eddy simulations," Quart. J. Roy. Meteor. Soc. **144**(716), 2182-2195 (2018).

[43]A. Haghshenas, J. P. Mellado, M. Hartmann, "Nonsingular zero-order bulk models of sheared convective boundary layers," J. Atmo. Sci. **76**, 3697-3715 (2019).

[44]A. K. Betts, "Reply to comment on the paper 'Non-precipitating cumulus convection and its parameterization'," Quart. J. Roy. Meteor. Soc. **100**(425), 469-471 (1974).

[45]E. Fedorovich. D. V. Mironov, "A model for a shear-free convective boundary layer with parameterized capping inversion structure," J. Atmo. Sci. **52**, 83-96 (1995).

[46]P. Liu, J. Sun, L. Shen, "Parameterization of sheared entrainment in a well-developed CBL. Part I: Evaluation of the scheme through large-eddy simulations," Adv. Atmo. Sci. **33**, 1171-1184 (2016).

[47]P. Liu, J. Sun, L. Shen, "Parameterization of sheared entrainment in a well-developed CBL. Part II: A simple model for predicting the growth rate of the CBL," Adv. Atmo. Sci. **33**, 1185-1198 (2016).

[48]J. C. R. Hunt, P. A. Durbin, "Perturbed vortical layers and shear sheltering," Fluid Dyn. Res. **24**(6), 375-404 (1999).

[49]A.-S. Smedman, U. Hogstrom, J. C. R. Hunt, "Effects of shear sheltering in a stable atmospheric boundary layer with strong shear," Quart. J. Roy. Meteor. Soc. **130**(596), 31-50 (2004).

[50]A.-S. Smedman, U. Hogstrom, J. C. R. Hunt, "Evidence of shear sheltering in atmospheric surface layer flow," in: A.J. Smits (Ed.), Proceedings of the IUTAM Symposium, IUTAM Symposium on Reynolds Number Scaling in Turbulent Flow, Princeton, NJ, 2002, 89-92.

[51]A. Haghshenas, J. P. Mellado, "Characterization of wind-shear effects on entrainment in a convective boundary layer," J. Fluid Mech. **858**, 145-183 (2019).

[52]H. R. Brand, R. J. Deissler, G. Ahlers, "Simple model for the Benard instability with horizontal flow near threshold," Phys. Rev. A **43**, 4262-4268 (1991).

[53]H. W. Muller, M. Lucke, M. Kamps, "Transversal convection patterns in horizontal shear flow," Phys. Rev. A **45**, 3714-3726 (1992).

[54]M. Tveitereid, H. W. Muller, "Pattern selection at the onset of Rayleigh-Benard convection in a horizontal shear flow," Phys. Rev. E **50**, 1219-1226 (1994).

[55]X. Nicolas, J.-M. Luijkx, J.-K. Platten, "Linear stability of mixed convection flows in horizontal rectangular channels of finite transversal extension heated from below," Int. J. Heat Mass Transf. **43**, 589-610 (2000).

[56]T.-F. Lin, "Buoyancy driven vortex flow and thermal structures in a very low Reynolds number mixed convective gas flow through a horizontal channel," Int. J. Heat Fluid Flow **24**, 299-309 (2003).

[57]Y. Requilé, S. C. Hirata, M. N. Ouarzazi, "Viscous dissipation effects on the linear stability of Rayleigh-Bénard-Poiseuille/Couette convection," Int. J. Heat Mass Transf. **146**, 118834 (2020).

[58]H. B. Squire, "On the stability of three-dimensional disturbances of viscous flow between parallel walls," Proc. Roy. Soc. London Ser. A. **142**, 621–628 (1933).

[59]P. Hazel, "Numerical studies of the stability of inviscid stratified shear flows," J. Fluid Mech. **51**, 39-61 (1972).

[60]C. B. Moler, G. W. Stewart, "An algorithm for generalzied matrix eigenvalue problems," SIAM J. Numer. Anal. **10**, 241-256 (1973).

[61]W. D. Smyth, D. J. Moum, J. D. Nash, "Narrowband, high-frequency oscillations at the equator. Part II: Properties of shear instabilities," J. Phys. Oceanogr. **41**, 412-428 (2011).

[62]Z. Liu, S. A. Thorpe, W. D. Smyth, "Instability and hydraulics of turbulent stratified

shear flows," J. Fluid Mech. **695**, 235-256 (2012).

[63]S. A. Thorpe, W. D. Smyth, L. Li, "The effect of small viscosity and diffusivity on the marginal stability of stably stratified shear flows," J. Fluid Mech. **731**, 461-476 (2013).

[64]Y. Xiao, W. Lin, "Linear temporal stability analysis on non-parallel free cross sheared flow with a primary hyperbolic velocity and an orthogonal Bickley jet velocity," Phys. Fluids **33**, 124101 (2021).

[65]Y. Xiao, W. Lin, "Linear temporal stability analysis on cross sheared flow: the stabilization effects via cross shear," Phys. Fluids **34**, 034101 (2022).

[66]P. G. Drazin, L. N. Howard, "Hydrodynamic stability of parallel flow of inviscid fluid," Adv. Appl. Mech. **9**, 1-89 (1966).

[67]W. D. Smyth, W. R. Peltier, "The transition between Kelvin–Helmholtz and Holmboe instability: an investigation of the overreflection hypothesis," J. Atmo. Sci. **46**, 3698-3720 (1989).

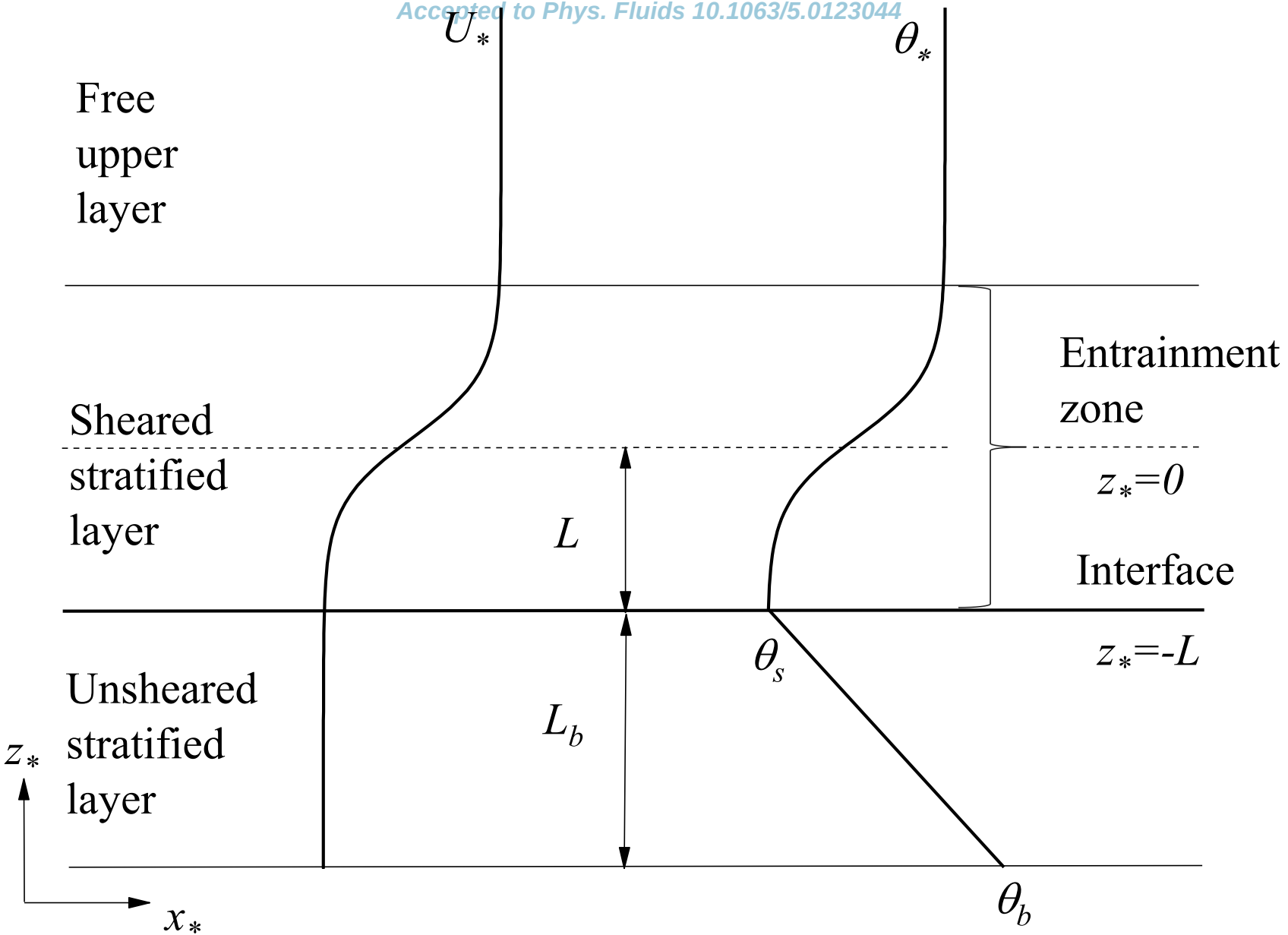

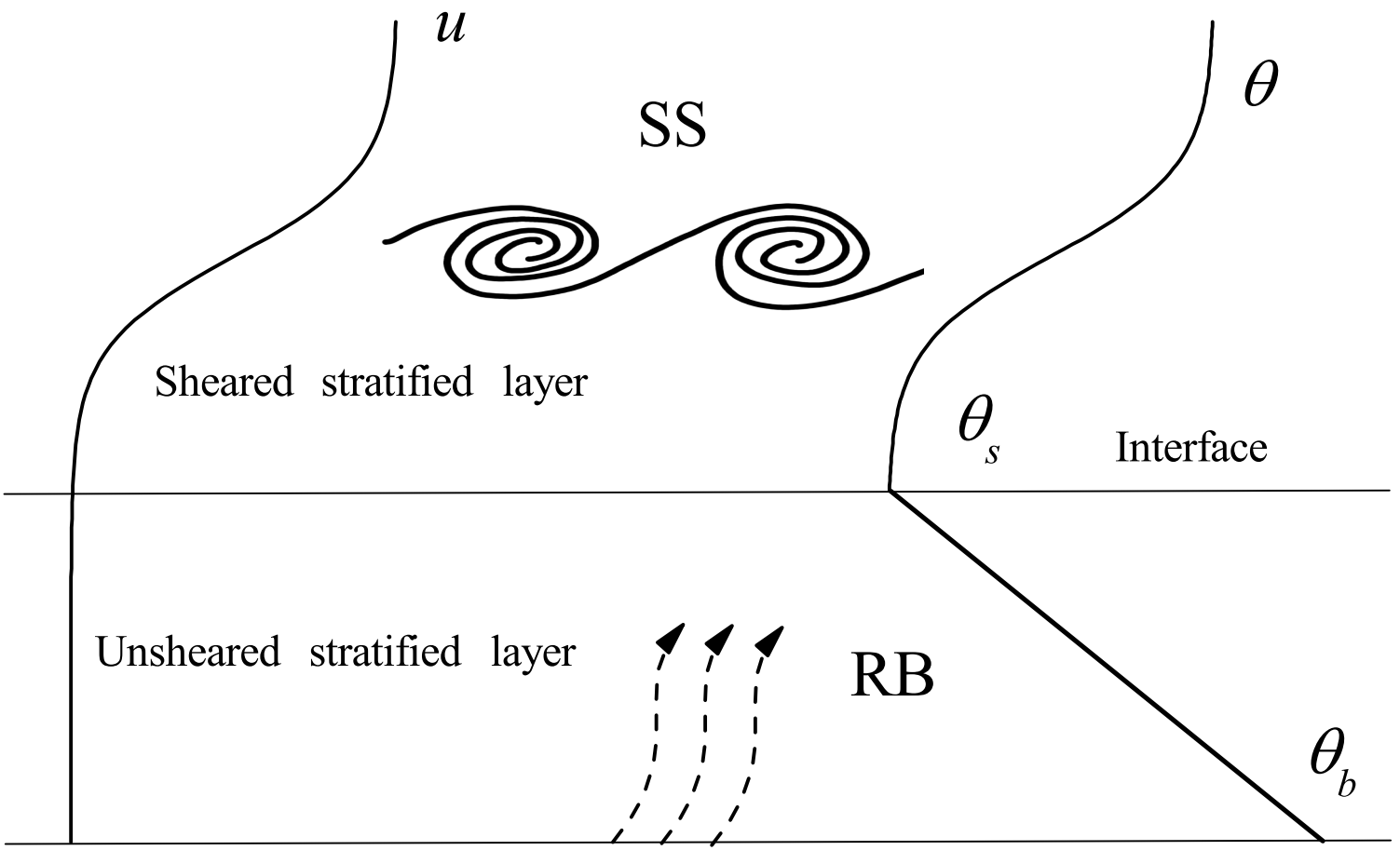

Accepted to Phys. Fluids 10.1063/5.0123044

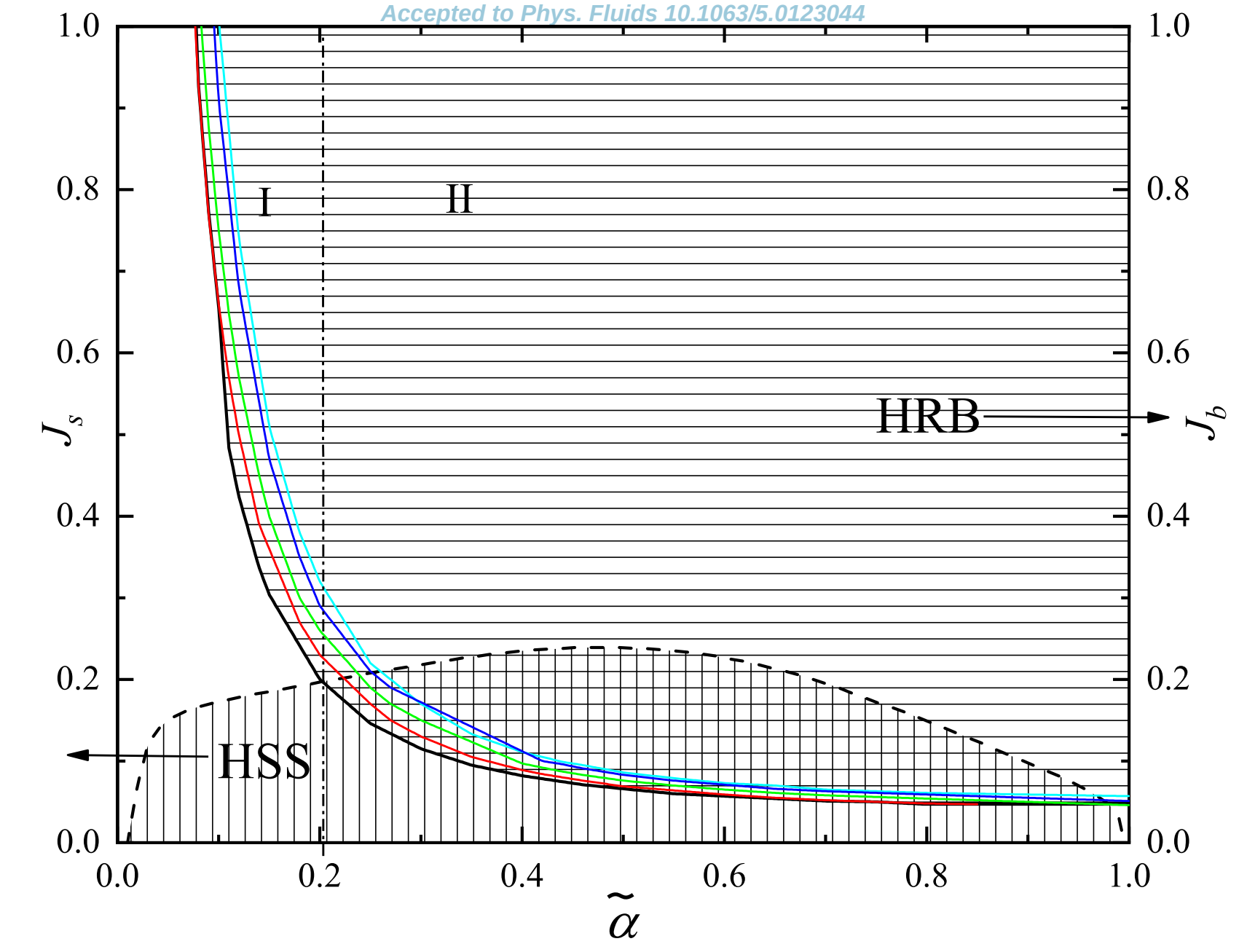

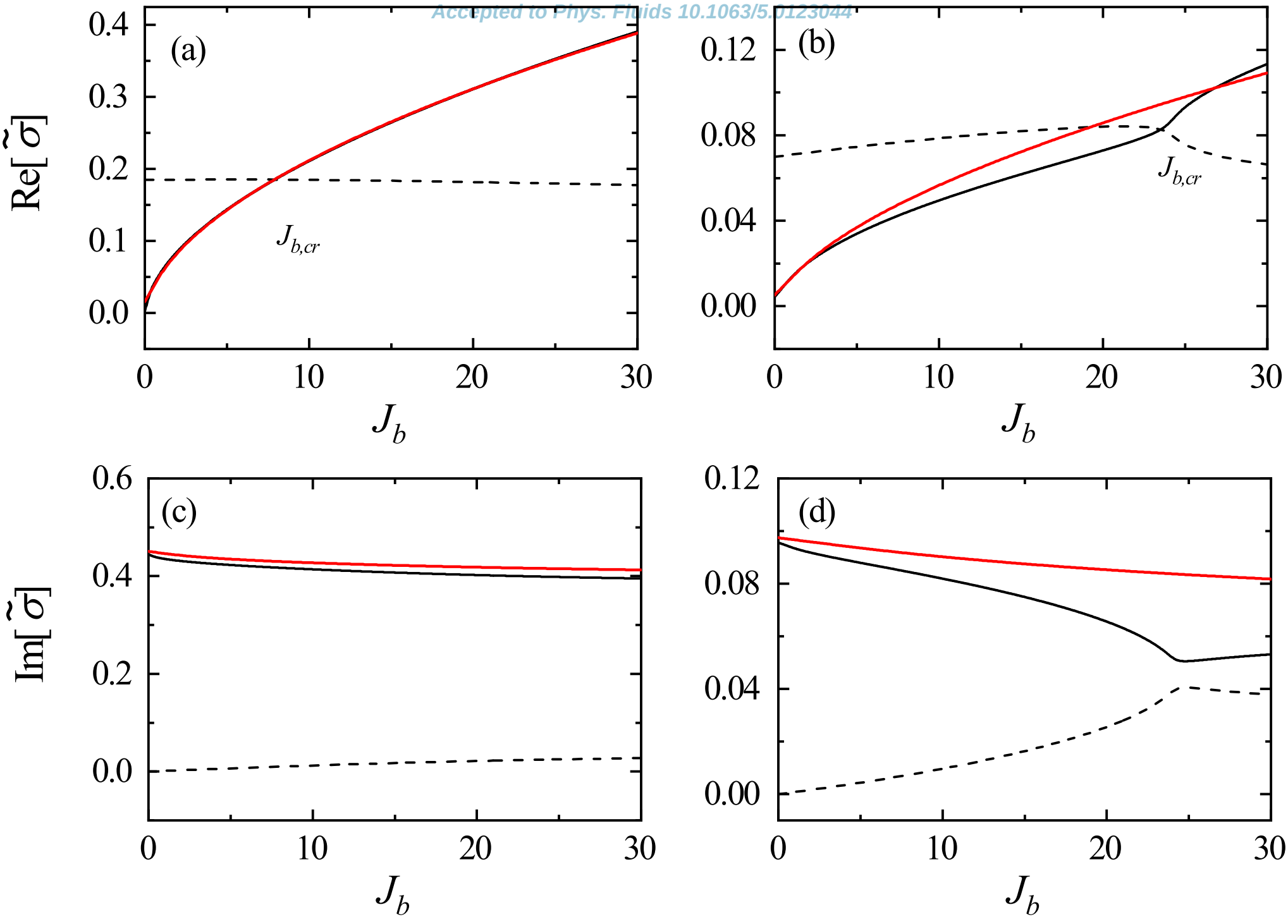

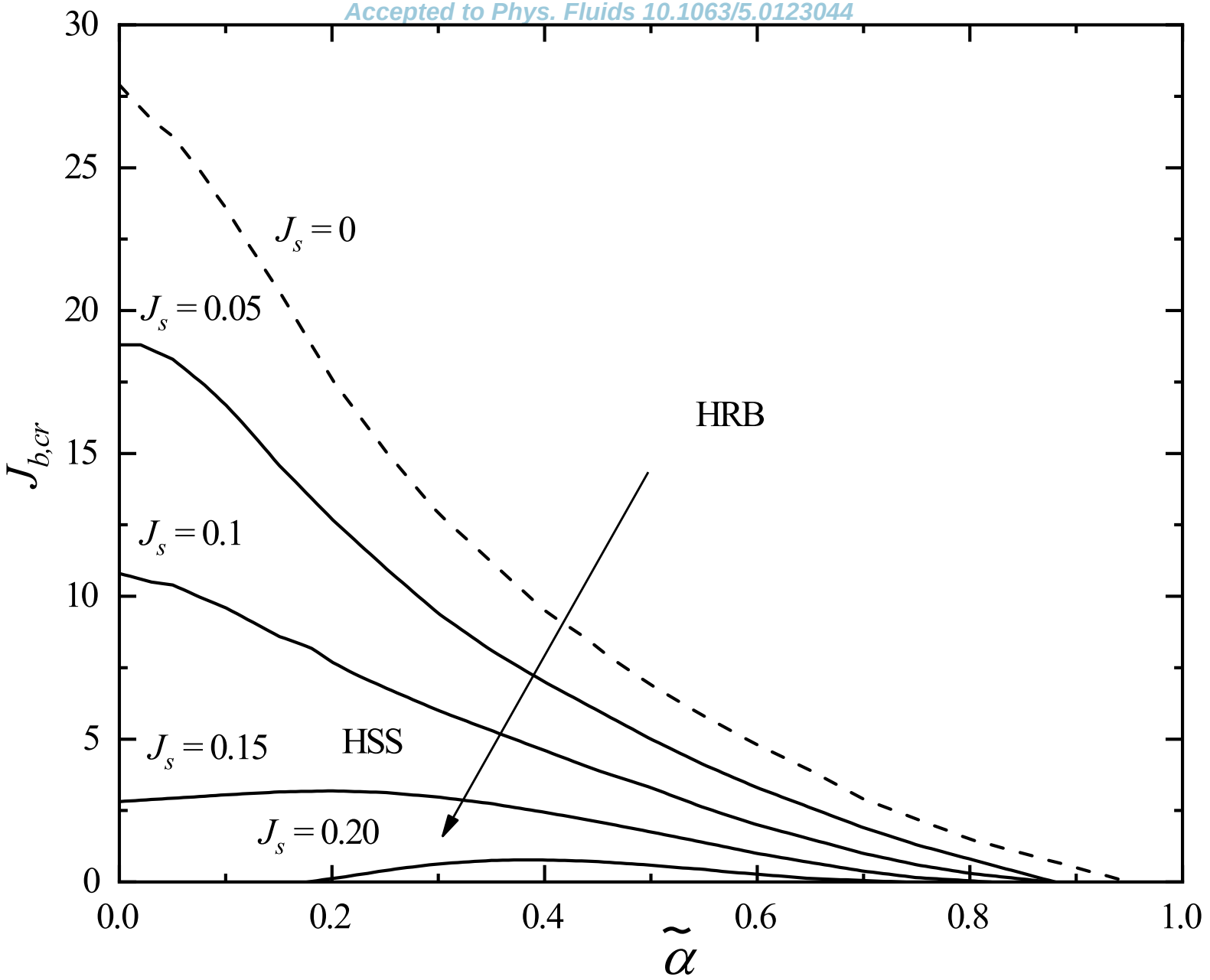

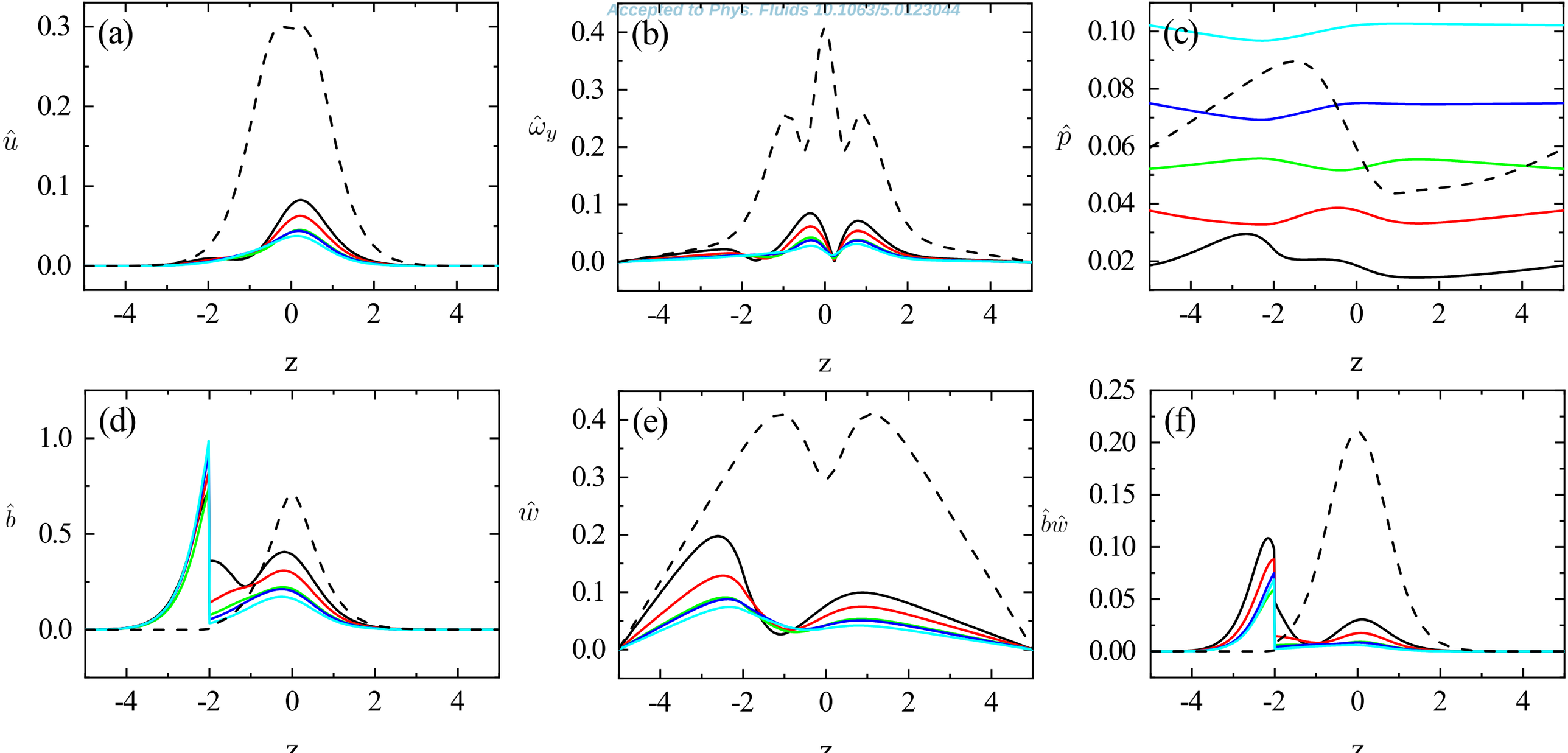

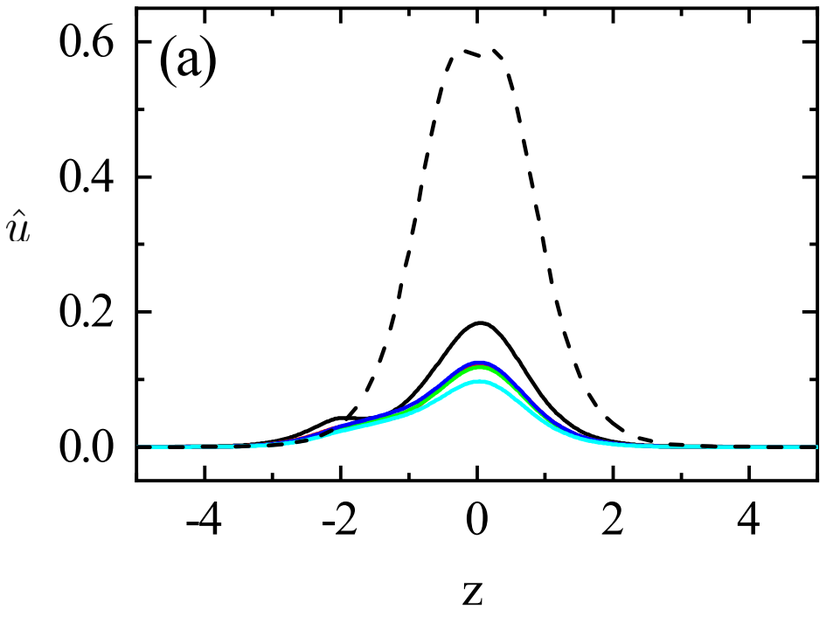

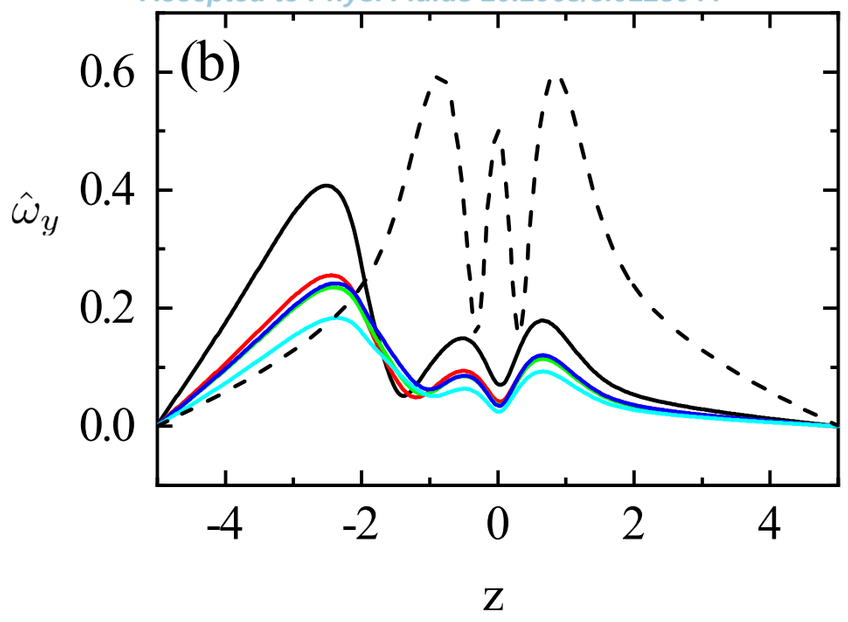

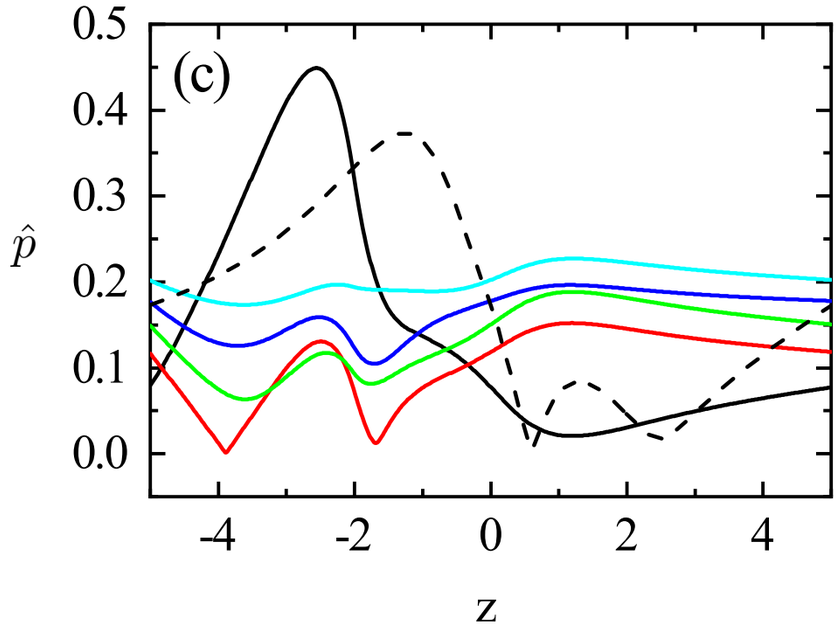

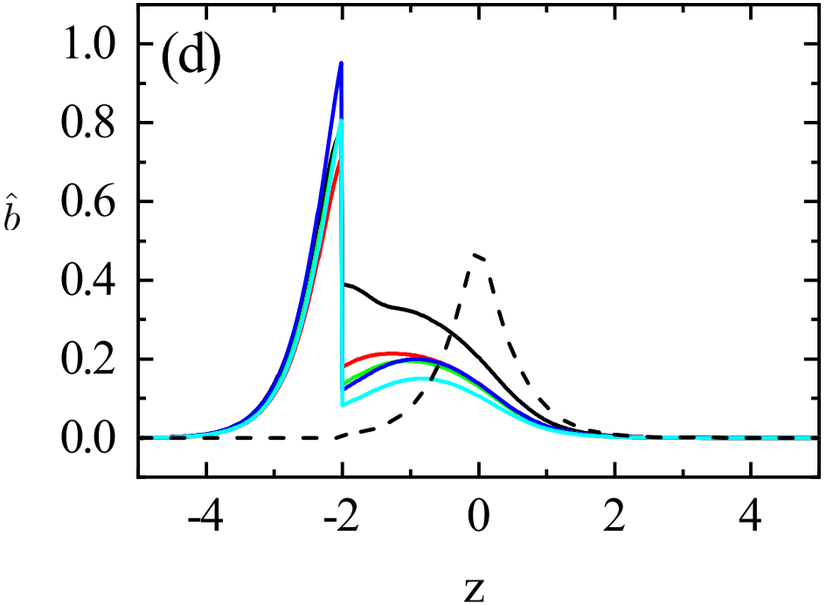

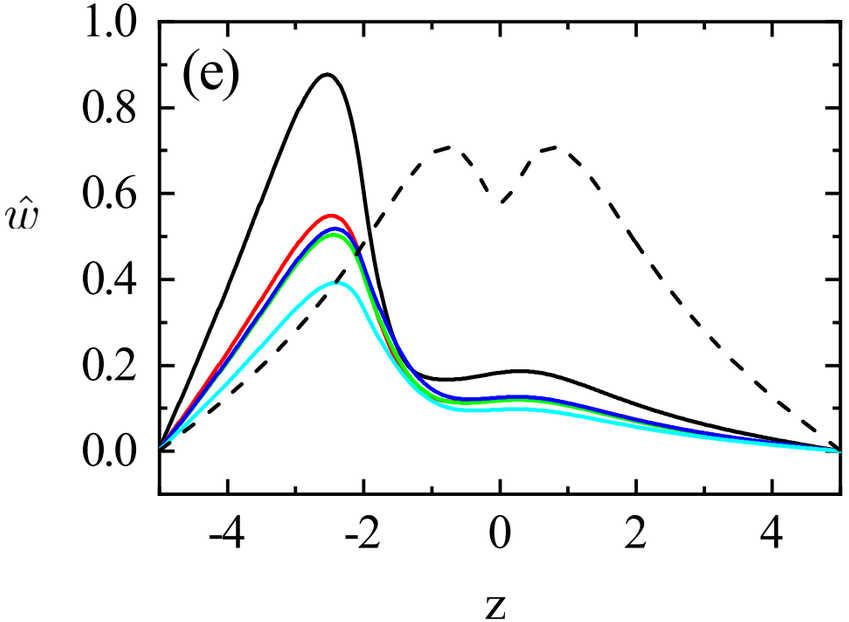

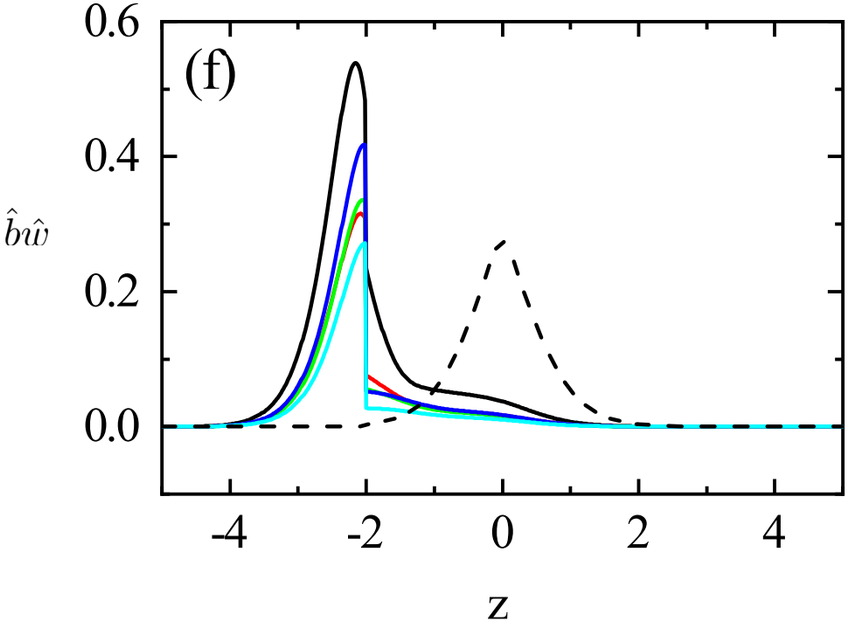

Accepted to Phys. Fluids 10.1063/5.0123044

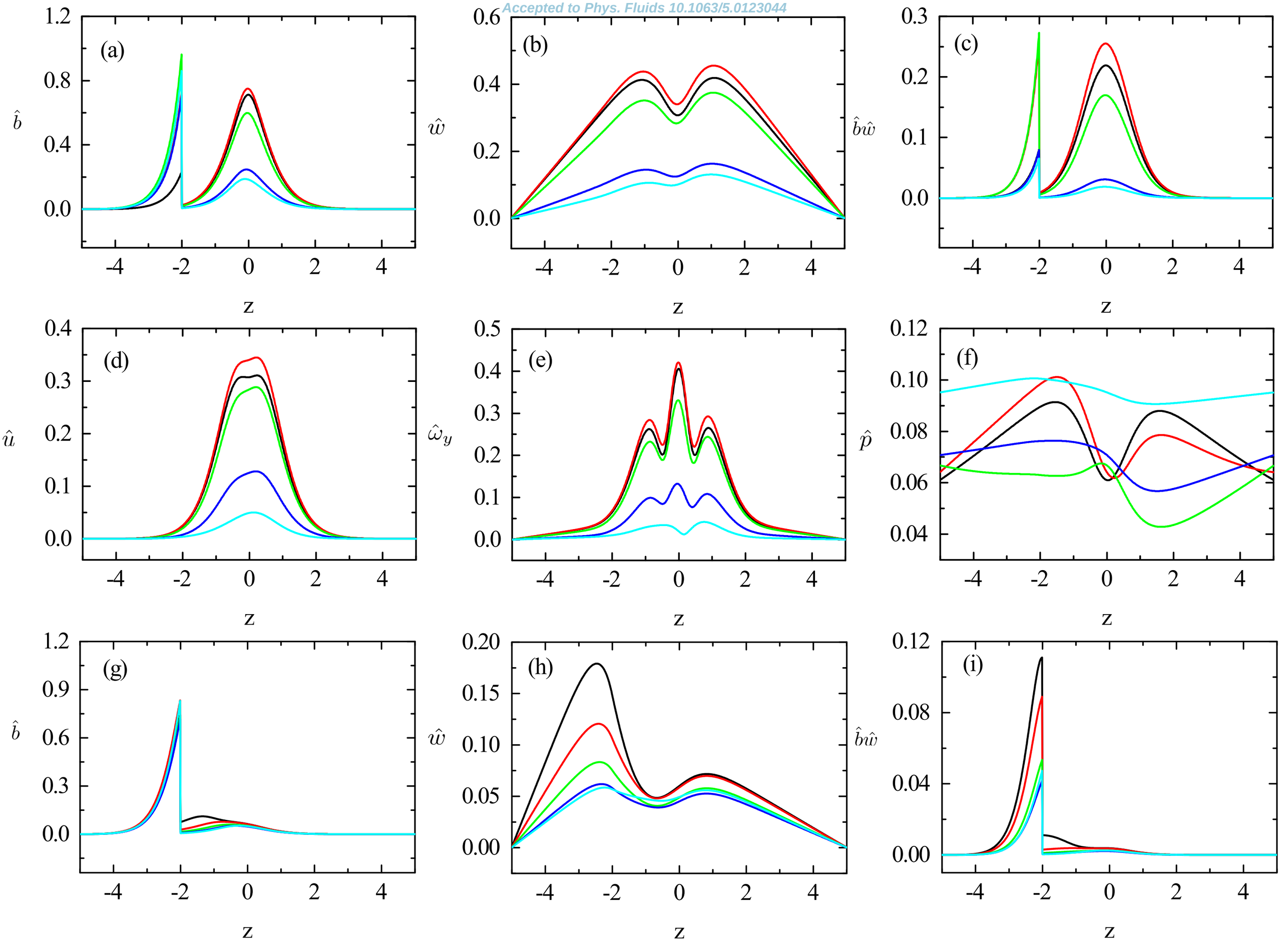

Accepted to Phys. Fluids 10.1063/5.0123044